



HAL
open science

Long-term growth of the Himalaya inferred from interseismic InSAR measurement

Raphael Grandin, Marie-Pierre Doin, Laurent Bollinger, Béatrice
Pinel-Puysségur, Gabriel Ducret, Romain Jolivet, S. N. Nath Sapkota

► **To cite this version:**

Raphael Grandin, Marie-Pierre Doin, Laurent Bollinger, Béatrice Pinel-Puysségur, Gabriel Ducret, et al.. Long-term growth of the Himalaya inferred from interseismic InSAR measurement. *Geology*, 2012, 40 (12), pp.1059 - 1062. 10.1130/G33154.1 . hal-01621509

HAL Id: hal-01621509

<https://hal.science/hal-01621509>

Submitted on 23 Oct 2017

HAL is a multi-disciplinary open access archive for the deposit and dissemination of scientific research documents, whether they are published or not. The documents may come from teaching and research institutions in France or abroad, or from public or private research centers.

L'archive ouverte pluridisciplinaire **HAL**, est destinée au dépôt et à la diffusion de documents scientifiques de niveau recherche, publiés ou non, émanant des établissements d'enseignement et de recherche français ou étrangers, des laboratoires publics ou privés.

Long-term growth of the Himalaya inferred from interseismic InSAR measurement¹

**Raphaël Grandin¹, Marie-Pierre Doin¹, Laurent Bollinger², Béatrice Pinel-
Puységur², Gabriel Ducret¹, Romain Jolivet³, and Soma Nath Sapkota⁴**

¹*Ecole Normale Supérieure, UMR 8538, F-75231 Paris, France*

²*CEA, DAM, DIF, F-91297 Arpajon, France*

³*Institut des Sciences de la Terre, UMR 5275, F-38041 Grenoble, France*

⁴*Department of Mines and Geology, National Seismological Centre, Lainchaur,
Kathmandu, Nepal*

ABSTRACT

The rise and support of the ~5000 m topographic scarp at the front of Indian-Eurasian collision in the Himalaya involves long-term uplift above a mid-crustal ramp within the Main Himalayan Thrust (MHT) system. Locking of the shallower portion of the flat-ramp-flat during the interseismic period also produces transient uplift above the transition zone. However, spatial and temporal relationships between permanent and transient vertical deformation in the Himalaya are poorly constrained, leading to an unresolved causal relationship between the two. Here, we use synthetic aperture radar interferometry (InSAR) to measure interseismic uplift on a transect crossing the whole Himalaya in Central Nepal. The uplift velocity of 7 mm/yr at the front of the Annapurnas is explained by a 18–21 mm/yr slip rate on the deep shallow-dipping portion of the MHT, with full locking of the mid-crustal ramp underlying the High Range. The transient uplift peak observed by InSAR matches spatially with the long-term uplift peak deduced from

¹ Article accepted for publication in *Geology* on 18 May 2012.

6
7
8

24 the study of trans-Himalayan rivers incision, although models of the seismic cycle
25 involving thrusting over a ramp of fixed geometry predict a ~20 km separation between
26 the two peaks. We argue that this coincidence indicates that today's mid-crustal ramp in
27 Central Nepal is located southward with respect to its average long-term location,
28 suggesting that mountain growth proceeds by frontward migration of the ramp driven by
29 underplating of material from the Indian plate under the Himalaya.

30 INTRODUCTION

31 Active thrusting of India under the Tibetan plateau gives rise to great earthquakes
32 that rupture the interseismically locked superficial portion of the Main Himalayan Thrust
33 (MHT) system (Fig. 1). In Nepal, uplifted Holocene terraces on the hanging wall of the
34 Main Frontal Thrust (MFT)—the southernmost branch of the MHT system—indicate that
35 nearly the whole 20 mm/yr convergence rate across the Himalaya is accommodated by
36 the MFT (Lavé and Avouac, 2001). Yet, the most prominent topographic step associated
37 with the continental collision, often called the physiographic transition 2 (PT₂), is located
38 ~100 km north of the MFT, at the front of the High Himalaya (Fig. 1). There, steep
39 topographic slopes coincide with a secondary local maximum in the bimodal long-term
40 uplift profile (Fig. 2). These features have been explained by the flat-ramp-flat geometry
41 of the MHT, with the localized zone of uplift in the hinterland marking the presence of an
42 underlying mid-crustal ramp (e.g., Cattin and Avouac, 2000). Another interpretation for
43 locally enhanced exhumation rates ~100 km north of the MFT relies on out-of-sequence
44 activation of a new fault partly coinciding with the Main Central Thrust (MCT)—the
45 northernmost branch of the MHT system—with the possible additional contribution of

10
11
12
46
47
48
49
50
51
52
53
54
55
56
57
58
59
60
61
62
63
64
65
66
67
68
13

intense rainfall along the orographic barrier (e.g., Hodges et al., 2004 ; Wobus et al., 2005).

During the interseismic period, the shallowest portion of MHT is locked. Constraining the location of the locking boundary within the MHT should permit us to pinpoint which up-dip portion of the MHT contributes most to long-term uplift in the Himalaya: a steep fault emerging near the MCT or the ramp-flat connection to MFT. Resolving this question could help to identify the most probable scenario among these two radically different views on the evolution of the Himalayan orogeny.

INSAR MEASUREMENT OF SURFACE VELOCITY FIELD

Using satellite-borne synthetic aperture radar interferometry (InSAR), we map the interseismic velocity field across the Himalayan range. In this region, the poor coherence is the primary obstacle to InSAR measurements. To tackle this issue, we apply a series of corrections that improve the spatial coherence of wrapped interferograms (see the GSA Data Repository¹). We use 29 C-band SAR images acquired between 2003 and 2010 over Western-Central Nepal. The images are precisely coregistered with respect to a single master image, and interferograms are computed using an a priori knowledge of topography to curb the impact of image distortion and limit geometrical decorrelation (Doin et al., 2011). A small-baseline strategy is implemented to take advantage of the redundancy on phase information and compensate for phase noise (Pinel-Puysségur et al., 2011). Digital elevation model (DEM) errors are determined by exploiting the proportionality between the perpendicular baseline and the local (wrapped) phase variability within the interferometric network (Ducret et al., 2011). Using independent atmospheric data provided by the ERA-Interim reanalysis of European Centre for

14
15
16

69 Medium-range Weather Forecast (ECMWF), we further correct the interferograms from
70 the contribution of stratified tropospheric delays (Jolivet et al., 2011). Corrected
71 interferograms are then filtered, unwrapped and geocoded. The impact of atmospheric
72 turbulence is reduced by the summation of 14 coherent interferograms, spanning a total
73 period of observation of 45 yr in the final line-of-sight velocity map (Fig. 1). Due to the
74 acquisition geometry, the resulting stack is insensitive to horizontal shortening across the
75 Himalaya, and primarily includes the contribution of the vertical component of the
76 deformation.

77 **INTERSEISMIC UPLIFT ACROSS THE HIMALAYA**

78 In the InSAR stack, we observe a band of uplifting terrain aligned with the trend
79 of the Himalaya, ~25 km south of highest peaks. This uplift signal shows no correlation
80 with surface elevation, indicating that the effect of tropospheric stratification has been
81 correctly compensated. We reference the deformation with respect to a stable Tibetan
82 plateau, where no notable interseismic deformation is observed. The location (~100 km
83 north of MFT), amplitude (5–7 mm/yr) and spatial wavelength (50 km) of the peak uplift
84 measured by InSAR are consistent with previous spirit leveling measurements in the
85 Kathmandu area (East-Central Nepal; see Fig. 1) (Bilham et al., 1997). In addition, a
86 remarkable agreement between the location of the band of uplifting terrain imaged by
87 InSAR and the microseismicity belt along the Main Himalayan Thrust is found (Pandey
88 et al., 1995). Finally, the maximum gradient of interseismic horizontal shortening
89 measured by the GPS in Central Nepal is co-located with the peak uplift detected with
90 InSAR, in agreement with theoretical expectations (Bettinelli et al., 2006). Therefore, the

17

18
19
20

91 geodetic data set combined here for the measurement of interseismic strain in Nepal

92 (InSAR, leveling and GPS) is internally consistent.

93 The simplest hypothesis on the cause of interseismic strain in Nepal is continuous
94 aseismic creep on the deep portion of the MHT, while its shallow portion from the
95 latitude of the high Range to the MFT is locked (Fig. 2) (Vergne et al., 2001). Here, we
96 model the creeping fault as a planar semi-infinite dislocation embedded in an elastic half
97 space (Okada, 1985), and we invert separately the geodetic data of East- and West-
98 Central Nepal to infer possible lateral variations in the configuration of the MHT. Fault
99 strike and rake are fixed to simulate a convergence direction of N10°E in West-Central
100 Nepal and N05°E in East-Central Nepal, which accounts for the curvature of the plate
101 boundary. Using a combination of horizontal (GPS) and vertical (InSAR or leveling)
102 data, we invert for the depth of the top of the dislocation, its dip angle, and its slip rate
103 using a nonlinear inversion method (Tarantola and Valette, 1982). The comparison of the
104 inversion results shows that fault geometry and slip rate cannot be distinguished between
105 East- and West-Central Nepal within the uncertainty of the data, suggesting that lateral
106 variations of the properties of the MHT in Central Nepal are small (Fig. 2). The preferred
107 model indicates that interseismic deformation is induced by a fault dipping at 3–7°,
108 buried at a depth of 20–24 km, with a slip rate of 18–21 mm/yr. This inferred deep
109 creeping portion of the MHT appears to correspond with a seismically imaged low-
110 velocity zone under southern Tibet (Nábělek et al., 2009). The up-dip projection of the
111 modeled dislocation intersects the surface well to the south of the active trace of the MFT
112 (see Fig. 2), suggesting that the MHT dips on average more steeply at seismogenic depth
113 than at greater depth in the stable-sliding domain. This is consistent with the flat-ramp-

21

22
23
24

114 flat geometry of the underlying MHT that has been inferred from the long-recognized
115 antiformal structure of the Lesser Himalaya (Fig. 2) (Schelling, 1992).

116 **DISCUSSION**

117 Current deformation measured by geodesy indicates that deep aseismic creep
118 terminates at the bottom of the mid-crustal ramp, which is consistent with full locking of
119 the ramp and frontal flat during the interseismic period. Great historical earthquakes are
120 believed to be caused by rupture of this locked portion of the fault system, thereby
121 compensating the deformation accumulated during the interseismic period. However, due
122 to the non-planar geometry of the MHT, permanent deformation is expected to remain
123 after each seismic cycle, which should be manifested by a net uplift centered above the
124 mid-crustal ramp. Therefore, if thrusting occurred over a mid-crustal ramp with a fixed
125 geometry, a ~20 km north-south separation should be observed between the transient
126 (interseismic, above the base of the ramp) and permanent (long-term, above the middle of
127 the ramp) peaks of uplift (Cattin and Avouac, 2000) (Fig. 3a).

128 On the other hand, the study of trans-Himalayan river profiles provides
129 constraints on the denudation processes that compete with this expected long-term uplift
130 (Lavé and Avouac, 2001; Seeber and Gornitz, 1983; Meade, 2010). This independent
131 geomorphological approach indicates that the locus of maximum long-term uplift is
132 actually situated at the same latitude as the interseismic uplift peak measured by geodesy
133 from InSAR and leveling (Fig. 2).

134 This spatial correspondence conflicts with the prediction, but can be accounted for
135 by several interpretations. Long-term and interseismic uplift could be collocated if
136 coseismic deformation related to slip on the MFT were not sufficient to compensate for

26
27
28

137 interseismic uplift (Bilham et al., 1997; Meade, 2010). Indeed, although
138 geomorphological evidence above the MFT indicate that nearly all of the shortening
139 between Tibet and India is accommodated at the front of the system, suggesting no or
140 little convergence deficit on the MFT (Lavé and Avouac, 2001), it is difficult to rule out
141 the possibility of a few mm/yr of permanent shortening in the High Himalaya. Thus, a
142 recently proposed mechanism is the out-of-sequence activation of a new thrust fault
143 intersecting the surface 0–35 km to the south of the mapped trace of MCT, and
144 outcropping near the break in topographic slope identified as a physiographic transition
145 (PT₂) (Wobus et al., 2005) (Figs. 1 and 3b). However, our inversions show that the base
146 of the locked portion of the MHT is located at a depth of ~20 km, between 0 km and 20
147 km to the South of PT₂ (Fig. 1). If a thrust fault connected PT₂ with the locking transition
148 of the MHT, then the observed spatial matching between long-term and interseismic
149 uplift would require an extremely high dip angle for this hypothesized fault (45–90°).
150 Such a steep dip angle would be incompatible with theoretical constraints on reverse fault
151 geometry provided by rock mechanics.

152 An alternative model of mountain building postulates that a strong topographic
153 gradient within the overriding block may be created by accretion of material from the
154 footwall to the hanging wall across the main thrust boundary (Fig. 3c) (Robinson et al.,
155 2003). Over several million years, numerical simulations of this underplating process
156 assume a continuous flux of material across the mid-crustal ramp (Bollinger et al., 2006).
157 However, on smaller time scales, accretion likely proceeds by discontinuous ramp jumps
158 toward the foreland, leading to the formation of a crustal-scale duplex (Schelling, 1992).
159 Migration of the ramp is expected to produce a gradual southward migration of the

160 topographic front that would tend to be competed by erosion. In the case of rapid erosion
161 processes, a steady-state situation should emerge, where the peak of long-term uplift,
162 which should roughly correspond to the location of the ramp, should be at any time
163 located south of the peak of transient interseismic uplift (Burbank et al., 2003). Yet, the
164 locus of maximum long-term denudation rate—which reflects the result of the
165 competition between erosion processes and rock uplift—appears to be located to the
166 north of the latitude of today's mid-crustal ramp inferred from our inversions, indicating
167 that the system is out-of-equilibrium. Alternatively, the observed coincidence between the
168 peak of interseismic uplift (marking the surface projection of the locked-to-unlocked
169 transition on the MHT) and the peak of long-term uplift (marking the average position of
170 the ramp over a period of time greatly exceeding the duration of a seismic cycle) could be
171 compatible with delayed erosional response to a recent southward migration of the ramp.
172 Assuming that a 20 km north-south offset between the two peaks is achieved when the
173 geometry remains fixed (Cattin and Avouac, 2000), and if erosion operates on time scales
174 of 0.1–1 m.y. (Lavé and Avouac, 2001), then the preservation of a coincidence between
175 the two peaks requires an apparent ramp migration velocity of 20–200 mm/yr. This rate
176 largely exceeds the average overthrusting rate of 5 mm/yr inferred from the thermal
177 structure of the Nepal Himalaya for the past 10 m.y. (Bollinger et al., 2006; Herman et
178 al., 2010). Therefore, our observations indicate that a southward jump of the mid-crustal
179 ramp has taken place recently in Central Nepal (83°E–86°E), adding support to the idea
180 that underplating, which is capable of maintaining the steep topography of the High
181 Himalaya on the long-term, is a discontinuous process in time. Resolving potential lateral
182 variations in the interseismic uplift pattern along the plate boundary is now required to

34
35
36

183 understand how the segmentation of the MFT, which ultimately controls the size of great
184 Himalayan earthquakes, could be related to the underlying long-term evolution of the
185 MHT system.

186 **CONCLUSIONS**

187 Mountain growth in the Himalaya is to a large extent controlled by the presence
188 of a mid-crustal ramp within the Main Himalayan Thrust system. Interseismic InSAR
189 measurements indicate that the ramp is locked during the interseismic intervals, causing
190 transient surface uplift above the transition zone. Over a large number of seismic cycles,
191 the flat-ramp-flat shape of the plate interface is expected to induce permanent uplift
192 above the ramp, whose surface expression is subdued by erosion, but which is
193 responsible for prominent topographic slopes and steep river profiles across the High
194 Himalaya. However, on the longer term, damage in the vicinity of the ramp produces
195 occasional brittle failure within the Indian plate that may bypass the MHT and lead to an
196 apparent southward migration of the mid-crustal ramp. Delayed erosional response to
197 such episodes of frontward ramp jump can produce the observed coincidence between the
198 peak of interseismic uplift detected by geodesy, and the peak of permanent uplift deduced
199 from riverbed morphology, which could not be otherwise explained by a steady-state
200 model of mountain growth.

201 **ACKNOWLEDGMENTS**

202 ENVISAT data was provided through European Space Agency's (ESA)
203 program Dragon-2. The seismic catalog was provided by National Seismological
204 Centre (NSC) of Nepal. Interferometric processing partly relies on the ROI_PAC
205 software (Rosen et al., 2004). Post-doctoral fellowship for Grandin was provided by

38
39
40

Publisher: GSA
Journal: GEOL: Geology
Article ID: G33154

206 French Centre National des Etudes Spatiales (CNES). We acknowledge funding from
207 Institut National des Sciences de l'Univers (CT-Risk), ESA's Young Scientist
208 Program and Agence Nationale de la Recherche (ANR) via project EFIDIR (ANR-
209 07-MDCO-004). This project was carried out within the frame of the joint ENS-CEA
210 laboratory "LRC Yves Rocard". We thank reviewers Roger Bilham, Roland
211 Bürgmann, and Tim J. Wright, and Editor Sandra J. Wyld for their useful comments.

212 REFERENCES CITED

- 213 Banerjee, P., Bürgmann, R., Nagarajan, B., and Apel, E., 2008, Intraplate deformation of
214 the Indian subcontinent: *Geophysical Research Letters*, v. 35, no. 18, p. L18301,
215 doi:10.1029/2008GL035468.
- 216 Bettinelli, P., Avouac, J.-P., Flouzat, M., Jouanne, F., Bollinger, L., Willis, P., and
217 Chitrakar, G.R., 2006, Plate motion of India and interseismic strain in the Nepal
218 Himalaya from GPS and DORIS measurements: *Journal of Geodesy*, v. 80, no. 8–11,
219 p. 567–589, doi:10.1007/s00190-006-0030-3.
- 220 Bilham, R. and 24 authors, 1997, GPS measurements of present-day convergence across
221 the Nepal Himalaya: *Nature*, v. 386, no. 6620, p. 61–64, doi:10.1038/386061a0.
- 222 Bollinger, L., Henry, P., and Avouac, J.P., 2006, Mountain building in the Nepal
223 Himalaya: Thermal and kinematic model: *Earth and Planetary Science Letters*,
224 v. 244, no. 1–2, p. 58–71, doi:10.1016/j.epsl.2006.01.045.
- 225 Burbank, D.W., Blythe, A.E., Putkonen, J., Pratt-Sitaula, B., Gabet, E., Oskin, M.,
226 Barros, A., and Ojha, T.P., 2003, Decoupling of erosion and precipitation in the
227 Himalayas: *Nature*, v. 426, no. 6967, p. 652–655, doi:10.1038/nature02187.

42
43
44
228
229
230
231
232
233
234
235
236
237
238
239
240
241
242
243
244
245
246
247
248
249
250

- Cattin, R., and Avouac, J.-P., 2000, Modeling mountain building and the seismic cycle in the Himalaya of Nepal: *Journal of Geophysical Research*, v. 105, no. B6, p. 13389–13407, doi:10.1029/2000JB900032.
- Doin, M.-P., Guillaso, S., Jolivet, R., Lasserre, C., Lodge, F., Ducret, G., and Grandin, R., 2011, Presentation of the small-baseline NSBAS processing chain on a case example: The Etna deformation monitoring from 2003 to 2010 using ENVISAT data: *Proceedings of the European Space Agency Symposium « Fringe »*, Frascati, Italy.
- Ducret, G., Doin, M.-P., Grandin, R., Lasserre, C., and Guillaso, S., 2011, DEM corrections before unwrapping in a small baseline strategy for insar time series analysis: *Proceedings of the IEEE International Geoscience and Remote Sensing Symposium*, Vancouver, Canada. (<http://www.ustream.tv/recorded/16259302>) (last accessed 25 April 2012).
- Feldl, N., and Bilham, R., 2006, Great Himalayan earthquakes and the Tibetan plateau: *Nature*, v. 444, no. 7116, p. 165–170, doi:10.1038/nature05199.
- Herman, F., Copeland, P., Avouac, J.-P., Bollinger, L., Mahéo, G., Le Fort, P., Rai, Foster, D., Pêcher, A., Stüwe, K. and Henry, P., 2010, Exhumation, crustal deformation, and thermal structure of the Nepal Himalaya derived from the inversion of thermochronological and thermobarometric data and modeling of the topography: *Journal of Geophysical Research*, v. 115, p. B06407, doi:10.1029/2008JB006126.
- Hodges, K.V., Wobus, C., Ruhl, K., Schildgen, T., and Whipple, K., 2004, Quaternary deformation, river steepening, and heavy precipitation at the front of the Higher Himalayan ranges: *Earth and Planetary Science Letters*, v. 220, p. 379–389, doi:10.1016/S0012-821X(04)00063-9.

46 Publisher: GSA
47 Journal: GEOL: Geology
48 Article ID: G33154
251 Jackson, M., and Bilham, R., 1994, Constraints on Himalayan deformation inferred from
252 vertical velocity fields in Nepal and Tibet: *Journal of Geophysical Research*, v. 99,
253 no. B7, p. 13897–13912, doi:10.1029/94JB00714.
254 Jolivet, R., Grandin, R., Lasserre, C., Doin, M.-P., and Peltzer, G., 2011, Systematic
255 InSAR tropospheric phase delay corrections from global meteorological reanalysis
256 data: *Geophysical Research Letters*, v. 38, p. L17311, doi:10.1029/2011GL048757.
257 Lavé, J., and Avouac, J.P., 2001, Fluvial incision and tectonic uplift across the Himalayas
258 of central Nepal: *Journal of Geophysical Research*, v. 106, no. B11, p. 26561–26591,
259 doi:10.1029/2001JB000359.
260 Meade, B.J., 2010, The signature of an unbalanced earthquake cycle in Himalayan
261 topography?: *Geology*, v. 38, no. 11, p. 987–990, doi:10.1130/G31439.1.
262 Nábělek, J., Hetényi, G., Vergne, J., Sapkota, S., Kafle, B., Jiang, M., Su, H., Chen, J.,
263 and Huang, B.-S., and the Hi-CLIMB Team, 2009, Underplating in the Himalaya-
264 Tibet collision zone revealed by the Hi-CLIMB Experiment: *Science*, v. 325,
265 no. 5946, p. 1371–1374, doi:10.1126/science.1167719.
266 Okada, Y., 1985, Surface deformation due to shear and tensile faults in a half-space:
267 *Bulletin of the Seismological Society of America*, v. 75, no. 4, p. 1135–1154.
268 Pandey, M.R., Tandukar, R.P., Avouac, J.P., Lave, J., and Massot, J.P., 1995, Interseismic
269 strain accumulation on the Himalayan Crustal Ramp (Nepal): *Geophysical Research*
270 *Letters*, v. 22, no. 7, p. 751–754, doi:10.1029/94GL02971.
271 Pinel-Puysségur, B., Michel, R., and Avouac, J.-P., 2011, Multi-link SAR interferograms:
272 Enhancement of a wrapped interferometric database: *Proceedings of the IEEE*
273 *International Geoscience and Remote Sensing Symposium*, Vancouver, Canada.

50
51
52

Publisher: GSA
Journal: GEOL: Geology
Article ID: G33154

- 274 Robinson, D.M., DeCelles, P.G., Garzione, C.N., Pearson, O.N., Harrison, T.M., and
275 Catlos, E.J., 2003, Kinematic model for the Main Central thrust in Nepal: *Geology*,
276 v. 31, p. 359–362, doi:10.1130/0091-7613(2003)031<0359:KMFTMC>2.0.CO;2.
- 277 Rosen, P.A., Henley, S., Peltzer, G., and Simons, M., 2004, Updated repeat orbit
278 interferometry package released: *Eos* [Transactions, American Geophysical Union],
279 v. 85, p. 47.
- 280 Schelling, D., 1992, The tectonostratigraphy and structure of the eastern Nepal Himalaya:
281 *Tectonics*, v. 11, no. 5, p. 925–943, doi:10.1029/92TC00213.
- 282 Seeber, L., and Gornitz, V., 1983, River profiles along the Himalayan arc as indicators of
283 active tectonics: *Tectonophysics*, v. 92, no. 4, p. 335–367, doi:10.1016/0040-
284 1951(83)90201-9.
- 285 Socquet, A., Vigny, C., Chamot-Rooke, N., Simons, W., Rangin, C., and Ambrosius, B.,
286 2006, India and Sunda plates motion and deformation along their boundary in
287 Myanmar determined by GPS: *Journal of Geophysical Research*, v. 111, no. B5,
288 p. B05406, doi:10.1029/2005JB003877.
- 289 Tarantola, A., and Valette, B., 1982, Generalized nonlinear inverse problems solved using
290 the least squares criterion: *Reviews of Geophysics and Space Physics*, v. 20, p. 219,
291 doi:10.1029/RG020i002p00219.
- 292 Vergne, J., Cattin, R., and Avouac, J.P., 2001, On the use of dislocations to model
293 interseismic strain and stress build-up at intracontinental thrust faults: *Geophysical*
294 *Journal International*, v. 147, no. 1, p. 155–162, doi:10.1046/j.1365-
295 246X.2001.00524.x.

296 Wobus, C., Heimsath, A., Whipple, K., and Hodges, K., 2005, Active out-of-sequence
297 thrust faulting in the central Nepalese Himalaya: *Nature*, v. 434, no. 7036, p. 1008–
298 1011, doi:10.1038/nature03499.

299 **FIGURE CAPTIONS**

300 Figure 1. **Vertical interseismic uplift in Central Nepal.** Map of Central Nepal showing
301 the main faults related to shortening across the Himalaya. MCT—Main Central Thrust;
302 MBT—Main Boundary Thrust; MFT—Main Frontal Thrust. The three branches merge at
303 depth with the Main Himalayan Thrust (MHT) dipping north under Tibet. Interferometric
304 synthetic aperture radar (InSAR) and leveling (Jackson and Bilham, 1994) measurements
305 of the vertical velocity are color coded from blue (subsidence) to red (uplift). White
306 circles represent the microseismic activity between 2000 and 2008 recorded by the
307 National Seismological Centre of Nepal. Small and large white triangles indicate the
308 location of the peaks with elevation above 7200 m and 8000 m, respectively (A—
309 Annapurna ; D—Dhaulagiri; M—Manaslu; X—Xishapangma). PT₂—physiographic
310 transition 2 (from Wobus et al. 2005).

311

312 Figure 2. **Geometry of the MHT.** Upper panel: profiles perpendicular to the mountain
313 range in West- (left) and East-Central Nepal (right) showing the horizontal velocities
314 derived from GPS and the vertical velocities derived from interferometric synthetic
315 aperture radar (InSAR) and leveling. Geodetic data have been projected along the profiles
316 indicated in Figure 1. Error bars denote 1 σ uncertainties on GPS velocities. Uncertainties
317 on leveling and InSAR are 0.2–2.8 mm/yr and 0.7–3.1 mm/yr, respectively. Colored
318 curves correspond to modeled interseismic deformation using a buried fault model. West-

58
59
60

Publisher: GSA
Journal: GEOL: Geology
Article ID: G33154

319 Central Nepal (red): dip = 6.5° ; depth = 24.1km ; slip rate = 20.6mm/yr. East-Central
320 Nepal (green): dip = 7.4° ; depth = 24.2km ; slip rate = 19.6mm/yr. The modeled
321 deformation in West-Central Nepal has been duplicated on the right panel for comparison
322 (dashed red line). Middle panel: stack of six denudation profiles determined from a study
323 of river incision (black line, Lavé and Avouac, 2001). Note that the same vertical scale is
324 used to represent interseismic uplift and denudation rates. The average topographic
325 profile is indicated in gray, with the envelope showing the minimum and maximum
326 elevations in an ~100-km-wide box centered on the main profiles. Lower panel: geometry
327 of the two inverted dislocations (red and green lines) represented on typical cross sections
328 showing the main faults at depth (STD—South Tibetan Detachment; ITSZ—Indus
329 Tsangpo Suture Zone) (Lavé and Avouac, 2001). The blue histogram shows the
330 distribution of seismic activity along the profile. Vertical exaggeration in the lower panel
331 is $2\times$.

332

333 **Figure 3. Seismic cycle, topographic construction and long-term evolution of the**
334 **MHT.** Three models showing the possible spatial relationship between interseismic uplift
335 profile (green curve at the top), long-term uplift profile (black curve at the top) and
336 microseismicity (blue histogram at the top) as a function of the underlying processes
337 taking place within the seismogenic crust.

338

339 ¹GSA Data Repository item 2012xxx, details of the InSAR processing scheme and
340 inversion procedure, is available online at www.geosociety.org/pubs/ft2012.htm, or on

62
63
64

Publisher: GSA
Journal: GEOL: Geology
Article ID: G33154

341 request from editing@geosociety.org or Documents Secretary, GSA, P.O. Box 9140,
342 Boulder, CO 80301, USA.

Figure 1

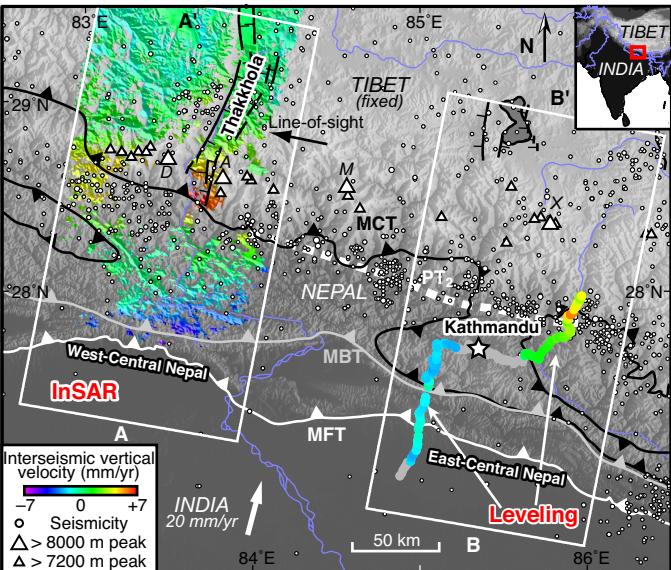


Figure 2

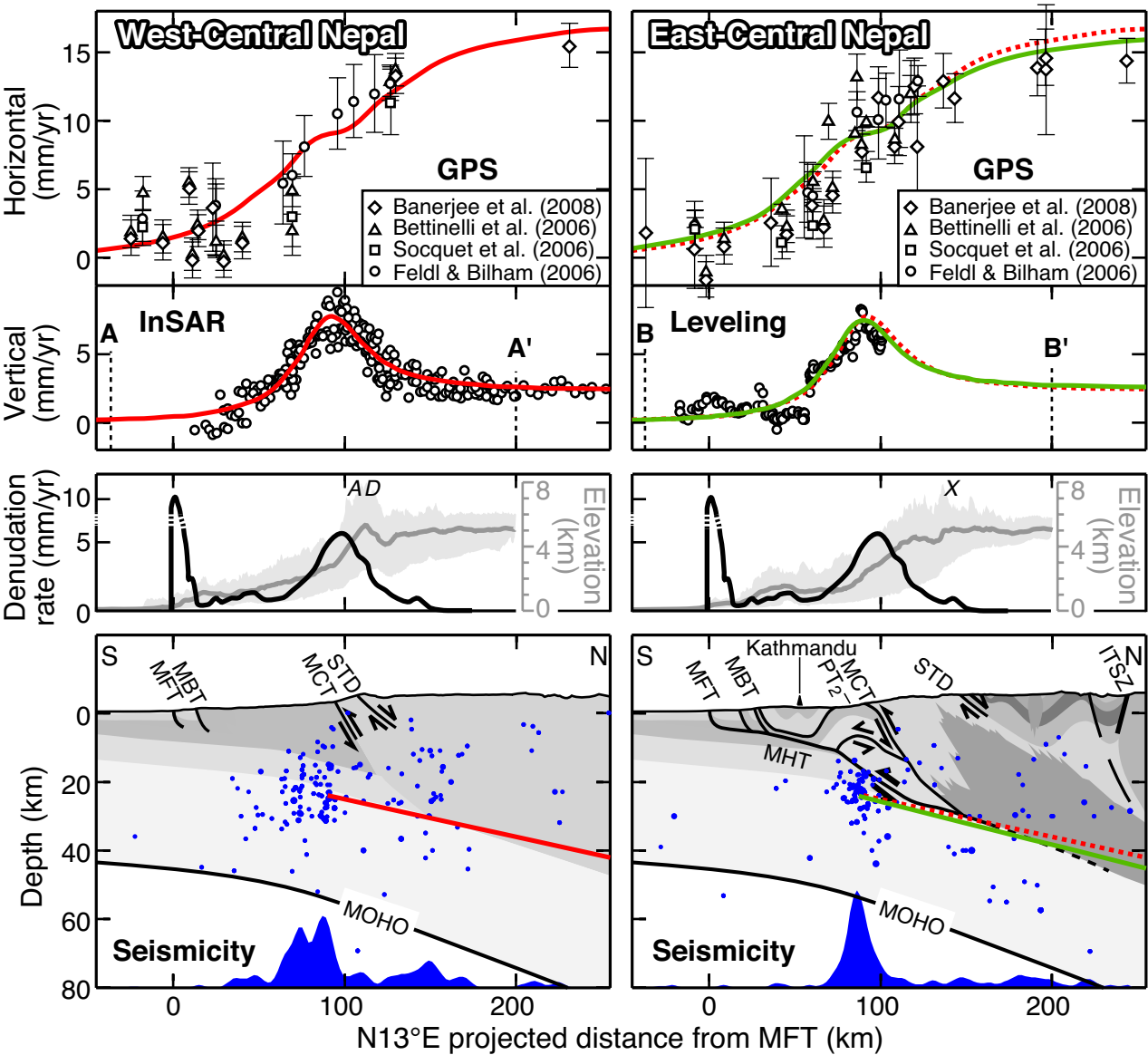
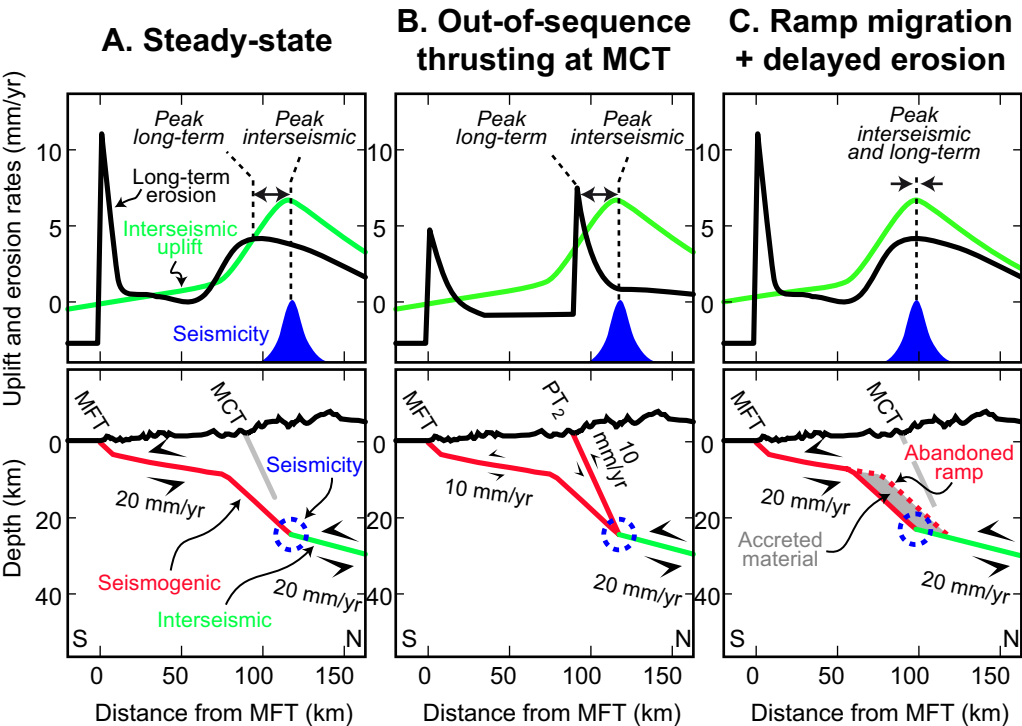


Figure 3



“Long-term growth of the Himalaya inferred from interseismic InSAR measurement”

R. Grandin, M.-P. Doin, L. Bollinger, B. Pinel-Puyssegur,
G. Ducret, R. Jolivet and S. N. Sapkota,

published in *Geology*

Supplementary information

Interferometric Synthetic Aperture Radar (InSAR) processing

The main difficulty opposed to InSAR studies in the Himalaya is the poor coherence of the area. A common method to enhance the coherence is interferogram multi-look. However, the combination of a rough topography and strong seasonality in the Himalaya induces large spatial and temporal variations of the tropospheric stratified delay, often producing tightly separated fringes that follow elevation contours in the interferograms [Jolivet *et al.*, 2011]. These fringes can be aliased if multi-look is applied to the interferograms. This results in complete coherence loss, contrary to the desired effect of multi-look. Previous attempts to measure ground deformation with InSAR in this region, which did not have a specific strategy to remove troposphere-related fringes prior to phase unwrapping, have encountered that problem.

In addition, other sources of errors should be corrected prior to unwrapping. These include digital elevation model (DEM) errors and phase noise. These perturbations can be handled using numerous SAR acquisitions, which is now possible thanks to the extensive ENVISAT archive accumulated since 2002, and the systematic acquisitions performed since 2008 in the Himalaya-Tibet area within the framework of European Space Agency’s (ESA) Dragon program. Finally, the rough topography

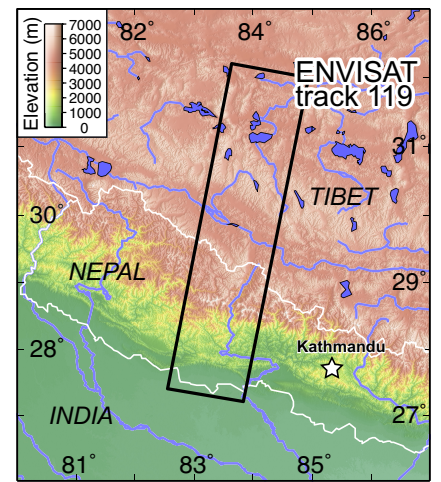


Figure S-1: Map showing the swath covered by ENVISAT track 119 used in this study.

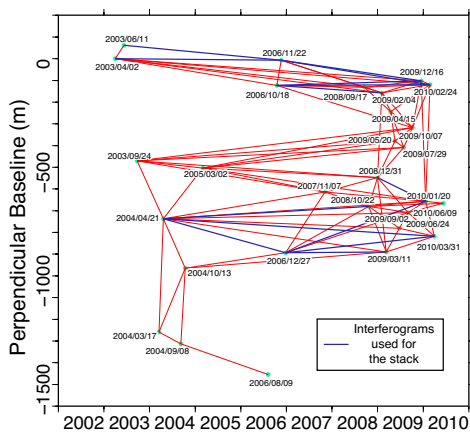


Figure S-2: Dates of image acquisitions as a function of perpendicular baseline. Red segments show the interferograms that have been calculated, among which blue segments show the interferograms used for the stack.

of the Himalaya leads to significant distortion of SAR images, even for modest perpendicular baselines between acquisitions. Correcting for this effect can substantially increase the number of usable interferograms.

In this study, we have applied a series of cascading corrections that aim at enhancing the coherence of wrapped interferograms prior to phase unwrapping. We computed interferograms from 29 ASAR images acquired by ESA’s ENVISAT satellite on track 119 (descending, IS2) between 2003 and 2010 (Figures S-1 and S-2). For interferogram calculations, we used a modified version of the ROI_PAC software [Rosen *et al.*, 2004] dedicated to a “small baseline” processing strategy (NSBAS processing chain [Doin *et al.*, 2011]). The doppler centroid was chosen to maximize the Doppler bandwidth overlap between images. A precise coregistration of all Single Look Complex images with respect to a single Master image was performed using an a priori distortion map in range derived from precise orbits and a digital elevation model (DEM). This step is crucial for the success of subsequent processing steps that rely on precise pixel matching among the different interferograms formed from the coregistrated SLCs. Here,

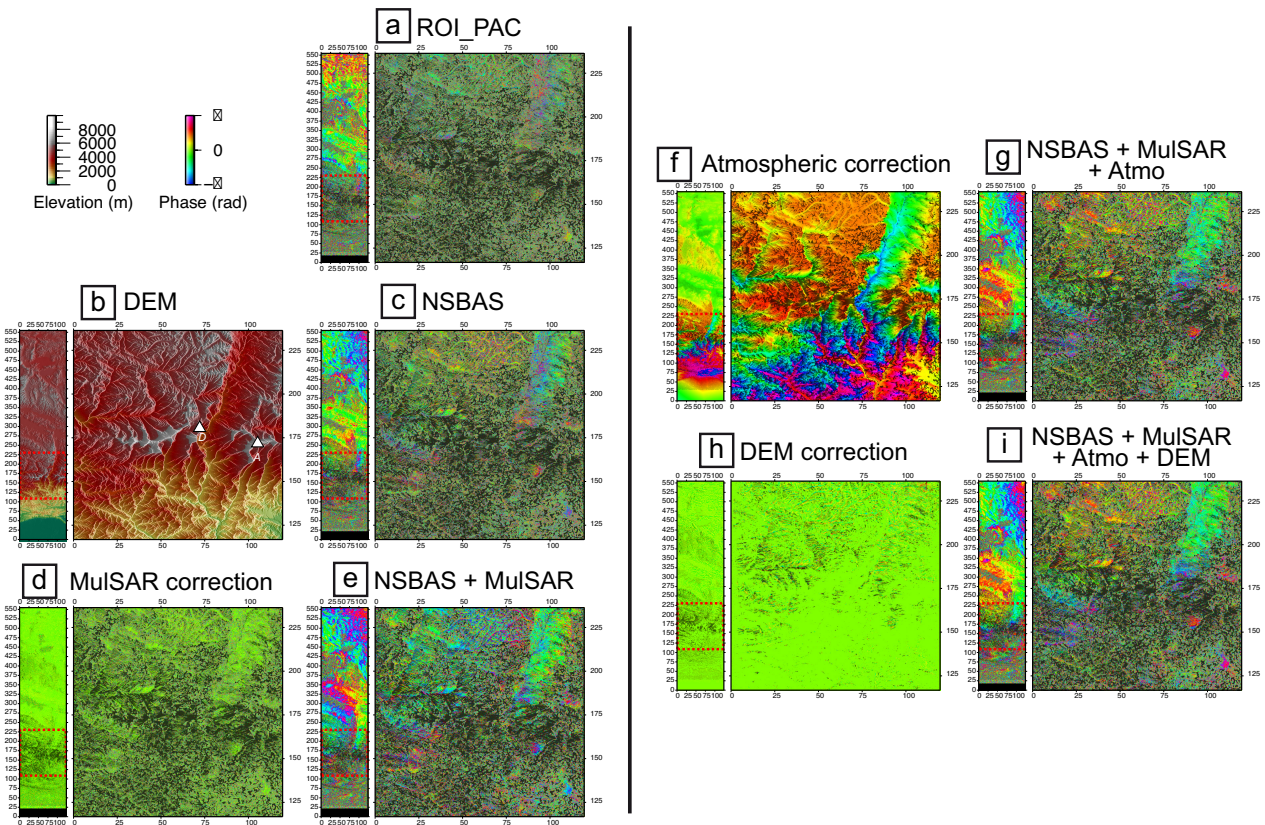


Figure S-3: Example of the effect of successive corrections applied prior to phase unwrapping. The example corresponds to an interferogram between 2006/12/27 and 2010/01/20 which was used in the stack. The temporal baseline of the interferogram is 3.06 years, and its perpendicular baseline is 236 m, which correspond to unfavourable conditions in terms of interferometric coherence. For each step, in order to highlight the impact of corrections on a broad scale and on a small scale, the interferogram spanning the whole swath (see Figure S-1 for location) is shown to the left of a blow up on the area with greatest topographic relief centered on the Himalaya (area surrounded by red dashed box). Areas in black in interferograms are incoherent regions where corrections are inefficient. (a) Interferogram processed with ROI_PAC. (b) SRTM-DEM in radar geometry. A: Annapurna. D: Dhaulagiri. (c) Interferogram processed with NSBAS [Doin et al., 2011]. (d) Correction for this interferogram determined after Multi-link InSAR time series (MulSAR) processing [Pinel-Puysségur et al., 2011]. (e) Interferogram after MulSAR correction. (f) Tropospheric delay correction computed from the ERA-Interim atmospheric model [Jolivet et al., 2011]. (g) Interferogram after atmospheric correction. (h) DEM correction calculated from combination of (wrapped) coherent interferograms with large perpendicular baselines and small temporal baselines [Ducret et al., 2011]. (i) Interferogram after DEM correction. Note the substantial improvement of the coherence between (a) and (i).

we used orbits derived from the onboard DORIS sensor [Zandbergen et al., 2003]. For the DEM, Version 4 of Shuttle Radar Topographic Mission Digital Elevation Model (SRTM-DEM-V4 [Farr et al., 2007]) was chosen because holes corresponding to the main Himalayan glaciers in previous versions of SRTM have been filled using regular topographic maps (data courtesy of Jonathan de Ferranti¹). In addition, a slope adaptive spectral shift range filtering was applied during interferogram formation to reduce geometric decorrelation caused by steep terrain slopes in the study area (implemented by S. Guillaso, following [Gatelli et al., 1994; Davidson and Bamler, 1999]). From the 29 co-registered SLCs, we computed 98 interferograms that allow for a fully connected interferometric network (Figure S-2). Calculated pairs include interferograms with a large temporal baseline (of direct interest for the measurement of interseismic deformation) but also images with a small temporal baseline and large perpendicular baseline (mainly used to connect between sets of images and to determine the DEM correction).

A series of cascading corrections were performed using the 4-look wrapped interferograms (i.e. 20-look in azimuth, 4-look in range) in order to enhance the coherence and reduce the risk of phase aliasing during the subsequent processing steps of multi-look and phase unwrapping. An example interferogram with a large temporal baseline (3.06 years) and a large perpendicular baseline (236 m) is shown in Figure S-3 to highlight the impact of these successive corrections. All wrapped interfero-

¹ <http://www.viewfinderpanoramas.org/dem3.html#himalayas>, last accessed 25 April 2012

grams were re-processed using the Multi-link InSAR time series scheme (MulSAR), which exploits the redundant information on the pixel phase by combining all the alternative paths between the master and slave image in the interferometric network, within the limit of three interferograms per path [Pinel-Puysségur et al., 2011] (Figure S-3 d-e). The resulting interferograms were then corrected from the effect of space-time variations of the stratified tropospheric component using the European Centre for Medium Range Weather Forecast (ECMWF) ERA-Interim meteorological reanalysis (Figure S-3 f-g). The method is described in detail in [Jolivet et al., 2011]. We note that the atmospheric correction provides the most important improvement; as it limits the aliasing of tightly separated topography-correlated fringes on the slopes of Himalaya in the later multi-looking step. Finally, DEM errors were calculated pixelwise by a non-linear inversion of the regression between perpendicular baseline and the (wrapped) interferometric phase, using the method of [Ducret et al., 2011] (Figure S-3 h-i). A subset of 36 interferograms with strong perpendicular baseline, small temporal baseline and good coherence

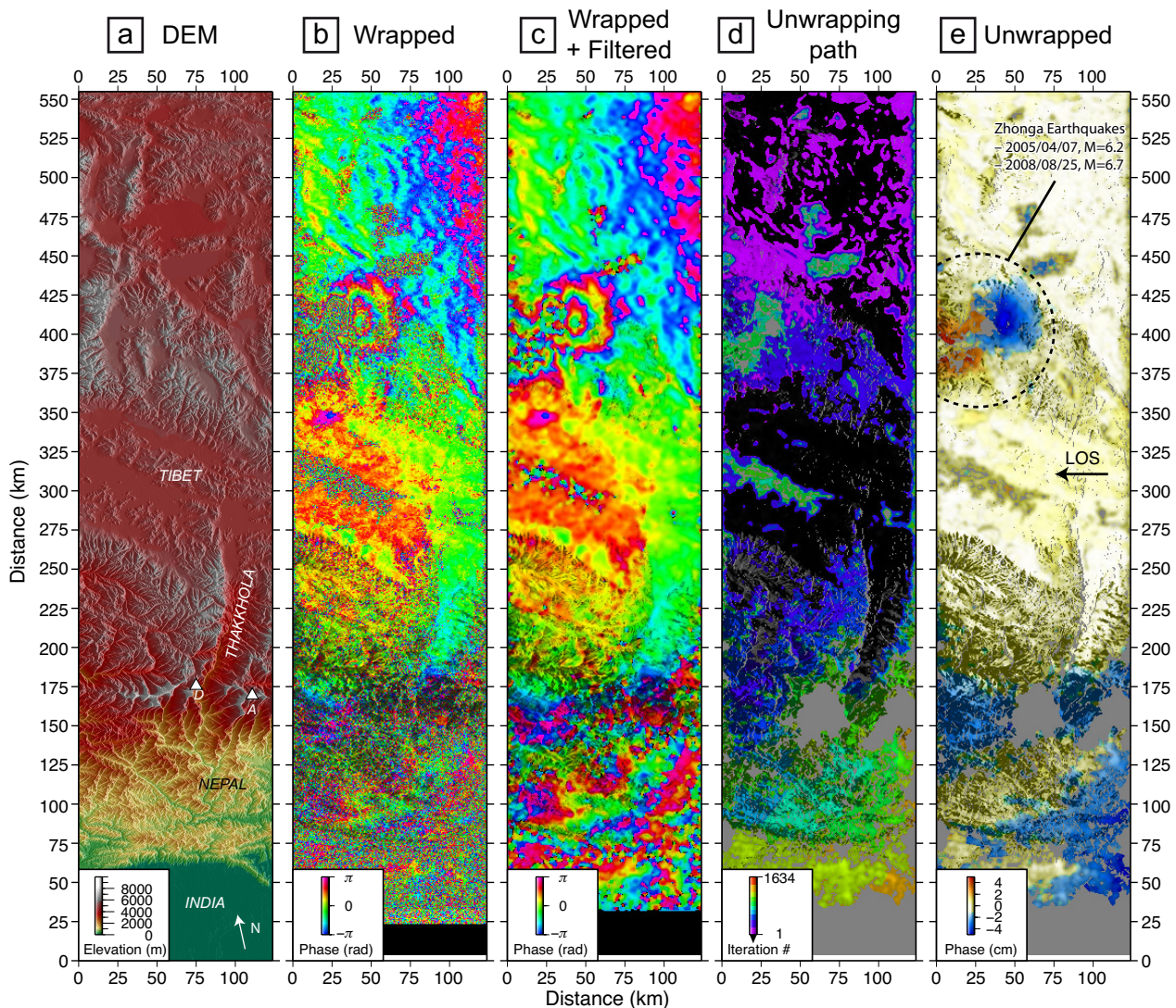


Figure S-4: Example of the process of filtering and unwrapping. The interferogram chosen for this example is the same as in Figure S-3. Areas in black are incoherent regions. (a) SRTM-DEM in radar geometry. (b) Wrapped interferogram after application of successive corrections aimed at enhancing the coherence (see Figure S-3). (c) Filtered, wrapped interferogram. (d) Unwrapping paths taken to propagate the unwrapping seed throughout the whole image during successive iterations corresponding to decreasing coherence thresholds. (e) Unwrapped interferogram. Unwrapping starts in areas coloured in black in (d), which correspond to areas of maximum coherence. Unwrapping then propagates toward regions of lower coherence, first in Tibet, then along the slopes of the Himalaya down to Nepal and India (bottom of the image). Two distinct unwrapping paths are found to cross the Himalaya: (1) along the western border of the image, and (2) along the Thakkhola graben between Dhaulagiri (D) and Annapurna (A). These two unwrapping paths merge in the Southern Thakkhola graben. No phase jump can be noticed at the junction of the two paths (e), indicating that unwrapping is not affected by large scale errors. In the upper part of the image, coseismic deformation associated with two earthquakes in 2005 and 2008 is also visible.

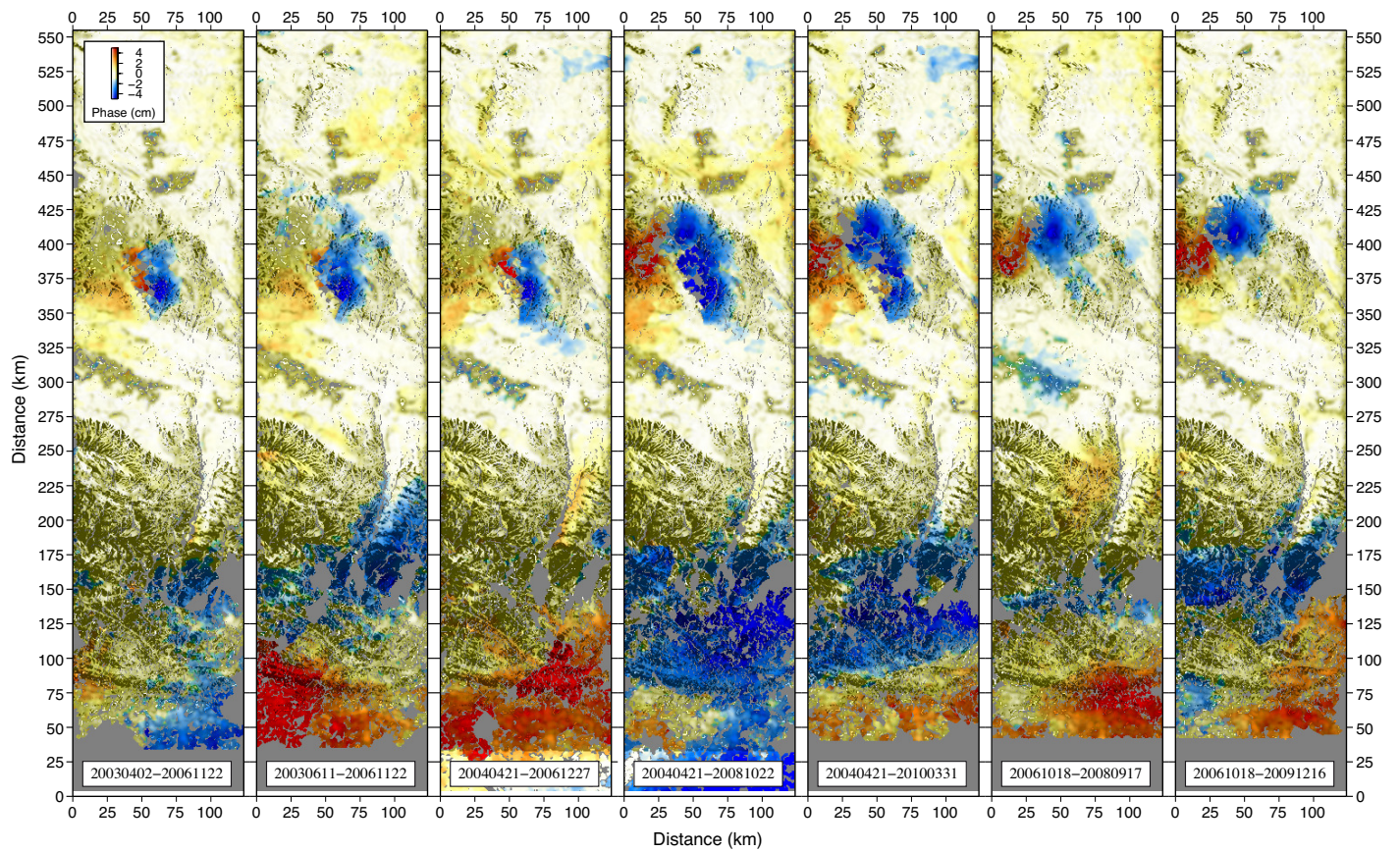


Figure S-5: Seven unwrapped interferograms among the 14 interferograms used in the stack. Interferograms are sorted as a function of the date of the first acquisition.

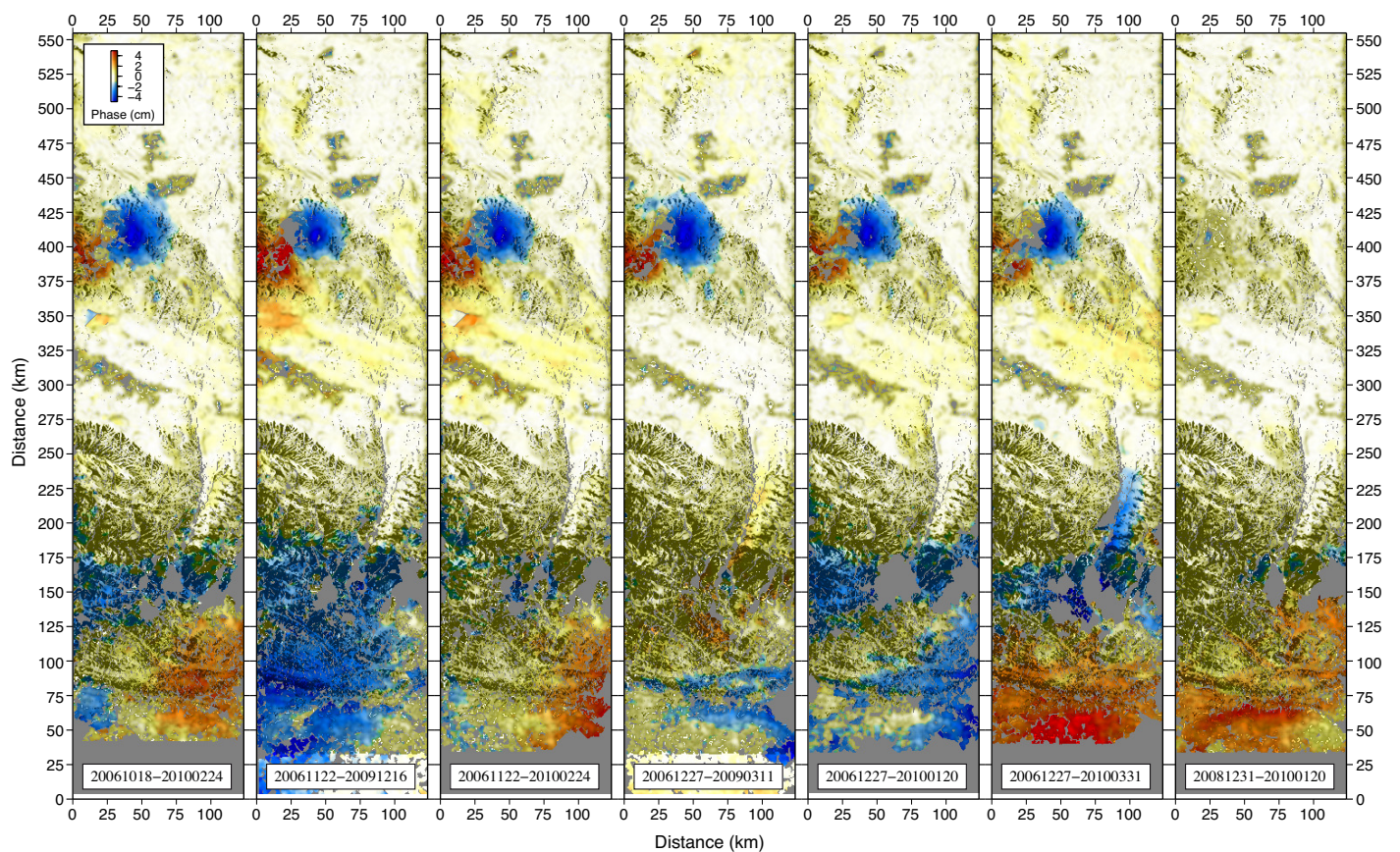


Figure S-6: Same as Figure S-5, for the seven remaining interferograms.

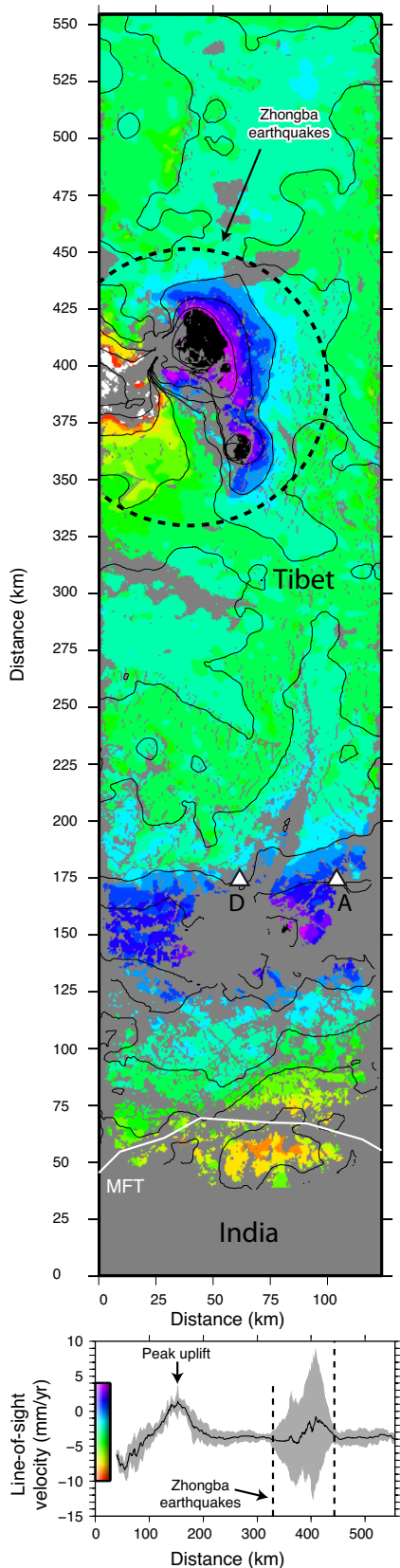


Figure S-7: Stack obtained by summation of unwrapped interferograms of Figures S-5 and S-6. Note that the average velocity has been calculated from pixels that have been correctly unwrapped for all 14 interferograms. Bottom panel shows a cross-section for a profile crossing the image along the satellite heading direction (azimuth direction), with the black curve corresponding to average line-of-sight velocity on each line, and the grey envelope showing 1σ standard deviation.

were used to determine the DEM error map, and the correction was subsequently applied to all other interferograms in the data set using their respective perpendicular baselines.

After these corrections, the resulting wrapped interferograms were multi-looked by an additional factor of 8 (i.e. leading to 32-look). Figure S-4 shows the unwrapping process applied to the example 32-look interferogram. To reduce phase noise, a 4-pixel wide triangular filter was applied to the wrapped 32-look interferograms, which represents a ~ 2.5 km-wide averaging kernel (Figure S-4 b-c).

Unwrapping is achieved in an iterative manner, using coherence as a criterion to determine an optimal unwrapping path (Figure S-4 d-e). The coherence used for unwrapping has been previously calculated in the same 4-pixel wide regions used for phase filtering. First, unwrapping is performed in the sub-region of the interferogram where coherence is maximum (i.e. with coherence above a certain threshold). At each iteration, the coherence threshold is slightly decreased, and unwrapping is propagated into the contiguous areas where coherence is above the new threshold. The threshold is progressively decreased to expand unwrapping toward regions of lower coherence at each iteration. Regions with a coherence below a minimum threshold are not unwrapped, as the phase is considered unreliable there. In addition, regions of spectral layover are assigned a very low coherence, and therefore behave as barriers that cannot be crossed during phase unwrapping (cuts). At each step, the unwrapping seed is propagated towards the region with the highest coherence, in order to favor unwrapping along the most coherent paths. Compared to cut-tree algorithm, our method accounts for the hierarchy in terms of phase reliability between regions with different levels of coherence. For example, our scheme tends to propagate unwrapping along coherent river valleys, and to avoid unwrapping to cross incoherent snow-capped mountain ridges which are unwrapped at the end of the process. The resulting interferograms are correctly unwrapped in the highly coherent region of the interferograms corresponding to Tibet, but errors tend to increase as unwrapping is propagated towards the South in Nepal. Coherence is smallest near the latitude of the high Himalaya, and is relatively higher to the South in the sub-Himalaya. Two separated unwrapping paths are usually found to connect Tibet and the sub-Himalaya: along the Thakkhola graben to the East of the track, and West of the Dhaulagiri Himal on the other side of the track (Figure S-4d). This makes possible to perform an a-posteriori check of the unwrapping reliability: if no phase jump is observed across either of the two low-coherence bottlenecks near the High Himalaya, then we can conclude that unwrapping has been achieved without producing a large-scale error. As a final step, unwrapped interferograms are geocoded.

Due to the overall poor coherence in the Himalaya, especially when the perpendicular baseline is high, only a small number of interferograms could be successfully unwrapped across the mountain range. Therefore, advanced post-processing techniques such as “small baseline” could not be applied to monitor time variations of the deformation. Instead, a simple stacking approach was adopted to highlight an average interseismic velocity map. We

selected a subset of 14 successfully unwrapped interferograms (including the contribution of 14 distinct images) that combine a large temporal baseline, a reasonably good coherence, and a reliable phase unwrapping (Figure S-2). These interferograms are shown in Figures S-5 and S-6. The interferograms were summed, and the result was divided by the total time spanned by the subset of interferograms (45 years in our case) in order to yield a line-of-sight (LOS) velocity map (Figure S-7). To compute the average velocity map, we chose a conservative approach by restricting the calculation to regions where all 14 interferograms have been successfully unwrapped. A “jackknife” analysis shows that the resulting velocity map is nearly insensitive to the exclusion of any interferogram among the list of 14 stacked interferograms.

We performed an error analysis to assess the amount of uncertainty affecting our final InSAR stack. For each interferogram used in the stack, we have computed semi-variograms of the residual LOS map after removal of the best-fit deformation model. Only the southern half of the InSAR swath was used, in order to highlight a noise level relevant to the area where interseismic deformation is observed (i.e. the Himalaya). The mean of the standard deviation of the interferograms at 50 km spatial wavelength (the

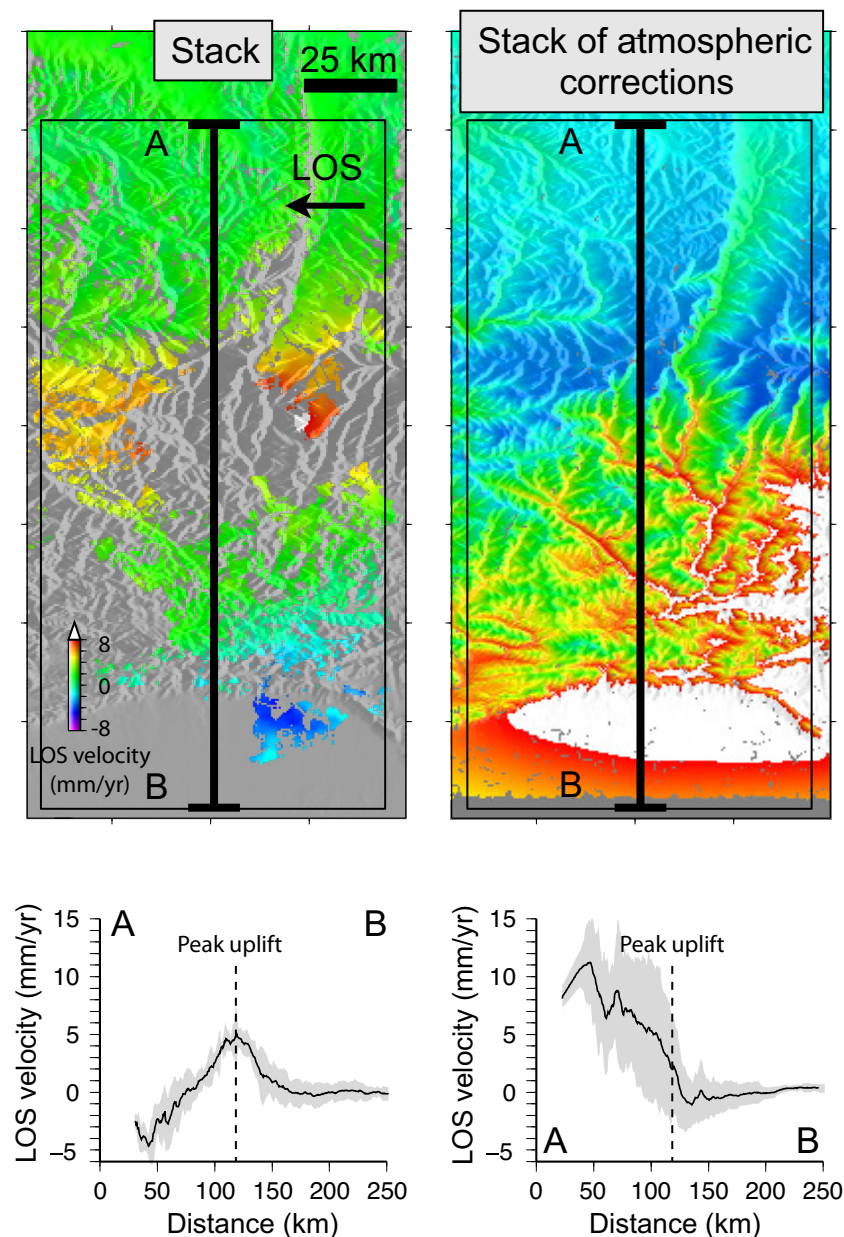


Figure S-8: Comparison between average LOS velocity map deduced from stack calculation (left) versus sum of the atmospheric corrections that have been subtracted from the 14 interferograms used to compute the stack (right). Bottom panel shows profiles along azimuth direction. The atmospheric correction is strongly correlated to elevation, whereas the retrieved LOS velocity map is unrelated to the distribution of elevations throughout the image, indicating that (1) the tropospheric delay contribution has been successfully removed from individual interferograms and (2) that the peak uplift obtained in the corrected stack was not introduced by inappropriate modeling of the tropospheric delay.

spatial wavelength of the uplift peak imaged by InSAR) was used as the reference standard deviation of any interferogram in the stack: $\sigma_{interf} = 21$ mm. From σ_{interf} , the average standard deviation of individual acquisitions σ_{acquis} is deduced by assuming that the variance of each interferogram equals the sum of the variances of the slave and master acquisitions. Hence, $\sigma_{acquis} = \sigma_{interf}/\sqrt{2} = 15$ mm. Finally, 10000 simulations of the noise in each acquisition were performed. Each acquisition was assumed to be the realization of a Gaussian random variable, with its mean equal to zero and its standard deviation equal to σ_{acquis} . The noise in the interferograms was then computed as the difference between the simulated noise amplitudes of slave and master acquisitions. The final noise amplitude in the average velocity map was calculated by reconstructing the stack (Figure S-2). The simulated noise in the stack was observed to follow a normal distribution centered at zero, with its standard deviation equal to $\sigma_{stack} = 3.1$ mm/yr. This compares to $\sigma_{stack} = 2.5$ mm/yr if the stack were composed of 14 independent interferograms. Such a level of uncertainty is likely an overestimation, as the best model of deformation is capable of fitting the InSAR data to a level of $\sigma_{residual} = 0.7$ mm/yr (Table T-1). We conclude that the uncertainty on the InSAR-derived velocity map lies in the range of 0.7–3.1 mm/yr.

The stack shows a region affected by motion toward the satellite with a peak located ~ 25 km South of the summits of the High Himalaya (Figure S-7). This signal appears to be uncorrelated with any topographic feature, as shown in Figure S-8. Because the chosen ENVISAT track is oriented parallel to the direction of India/Tibet convergence (descending track), the LOS measurement is virtually insensitive to horizontal displacements related to shortening perpendicular to the Himalayan range. Therefore, the LOS velocity map is converted to a vertical velocity map by dividing by the cosine of the incidence angle (between 19° for the near-range and 26° for the far-range). The band of LOS velocity directed toward the satellite is interpreted as a direct measurement of uplift caused by interseismic contraction of rocks above the transition zone between the locked and free slipping portions of the Main Himalayan Thrust (MHT). The peak uplift velocity is approximately 5–7 mm/yr. The amplitude and wavelength of the signal are consistent with leveling measurements of interseismic uplift in the Kathmandu area [Jackson and Bilham, 1994]. Further to the South, moderate motion away from the satellite (possibly subsidence) is observed, but this signal is considered unreliable South of the MFT due to suspected unwrapping errors across the MFT. Therefore, InSAR data South of the MFT has not been used in the inversions. The stack also includes coseismic deformation associated with the Zhongba earthquakes of 11/07/2004 ($M = 6.2$), 07/04/2005 ($M = 6.2$) and 25/08/2008 ($M = 6.7$) in the Tibet interior (Figures S-3, S-5, S-6 and S-7). The average velocity in this area is therefore meaningless for the description of interseismic deformation, and has been clipped. Elsewhere in Tibet, the resulting velocity map shows no notable deformation. A bilinear phase ramp is adjusted in the region located North of 29°N , and then subtracted to the whole InSAR stack, in order to reference the deformation with respect to a stable Tibetan plateau. The slight longitudinal difference in uplift velocities within the InSAR track could be interpreted as lateral variability of the underlying fault properties, with more interseismic coupling, a shallower locking depth below the eastern part of the track compared to the western part of the track, and/or extension within the Thakkhola graben. However, the difference in uplift velocity is within the uncertainty of the InSAR measurement (~ 2 mm/yr), and cannot be interpreted further.

Leveling data

To complement InSAR measurement in West-Central Nepal, we also use spirit leveling measurements in the East-Central Nepal region (Kathmandu area) reported by [Jackson and Bilham \[1994\]](#) and originally measured by the Survey Department of Nepal since 1977 (Figure S-9). The leveling survey was performed along a 350 km-long line, trending roughly North-South, and crossing the MFT, the MBT and the MCT. However, due to an east-west jog of nearly 60 km in the profile at the latitude of Kathmandu, the range-perpendicular coverage of the profile is only 130 km. The leveling profile shows a gentle increase of the uplift rate toward the North, with a peak uplift reached ~ 90 km North of the MFT. The lower part of the profile was revisited after an interval of 13 years, whereas the upper part of the profile spans 7 years of deformation, and only 2 years for the uppermost part of the profile, i.e. North of the peak uplift. Unfortunately, the profile ends only 10 km North of the peak uplift. In our analysis, outliers in the Kathmandu valley and lowlands have been removed, following [Bettinelli et al. \[2006\]](#).

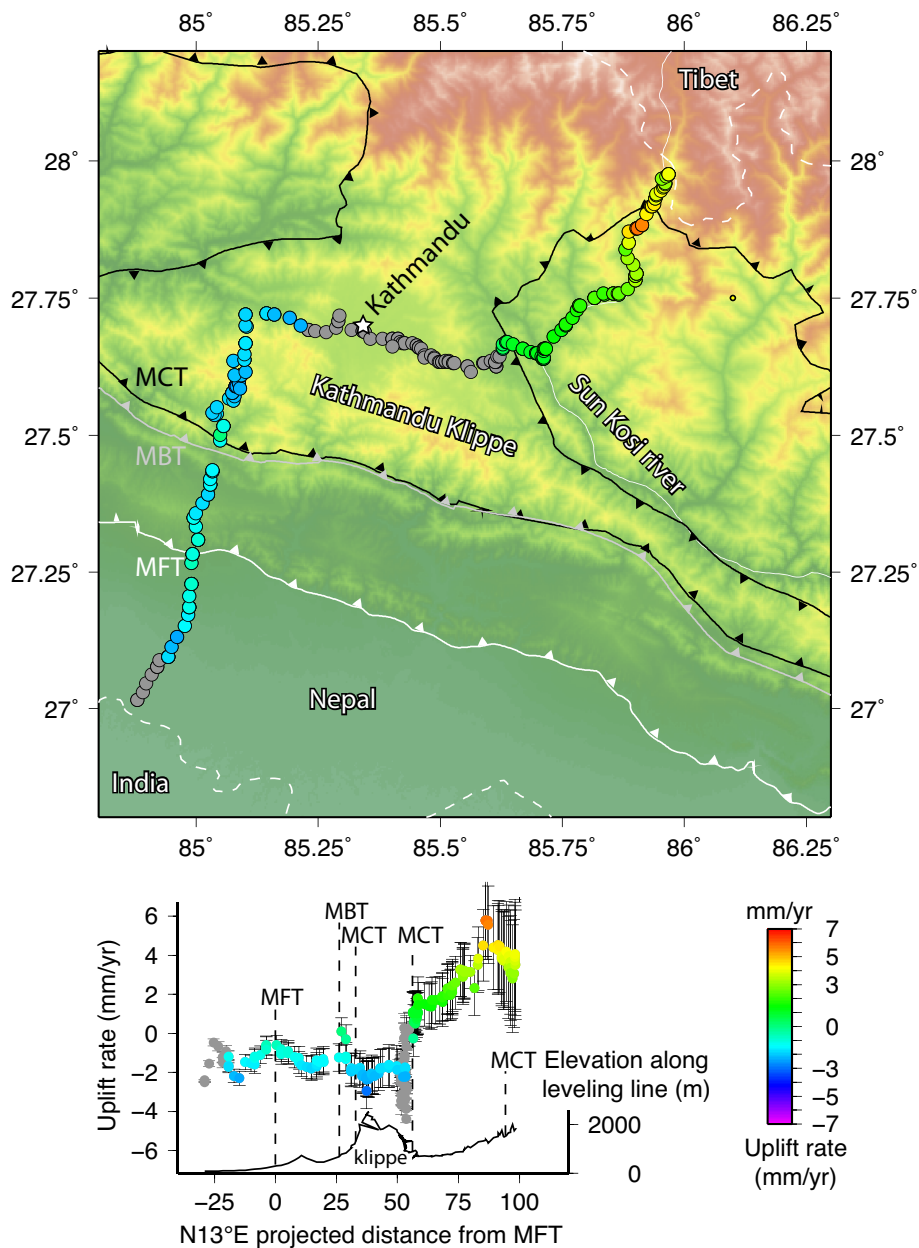


Figure S-9: Leveling data used in this study [[Jackson and Bilham, 1994](#)]. Top: map of the leveling profile overlaid on a DEM of the Kathmandu area. Vertical velocity is color coded from blue (subsidence) to red (uplift). Data points in grey correspond to measurements affected by subsidence in the Kathmandu valley that have been discarded from the inversion input. In its upper part, the profile follows the Sun Kosi river, which is indicated in grey. Bottom: vertical velocity along the leveling profile projected along a N13°E direction, with the origin of the x-axis set to the MFT. Error bars correspond to 1σ standard deviation uncertainties. Elevation along the leveling line is indicated below.

Global Positioning System (GPS) data

To constrain the horizontal component of the interseismic velocity field, we focus on four GPS data sets published by *Bettinelli et al.* [2006], *Socquet et al.* [2006], *Feldl and Bilham* [2006] and *Banerjee et al.* [2008]. These data sets provide a good spatial coverage of the region imaged by InSAR in West-Central Nepal, as well as dense coverage in the Kathmandu area in East-Central Nepal where the leveling line was measured. The data consist of a few continuous GPS stations operated since 1997 jointly by the Nepalese Department of Mines and Geology (DMG) and French CEA-DASE in the Kathmandu area. However, most GPS measurements were carried out during campaign surveys by teams of the Cooperative Institute for Research in Environmental Sciences, University of Colorado (CIRES), French Centre National de la Recherche Scientifique (YDIL-Him), DASE and DMG. The first measurements were performed in 1991 in West-Central Nepal, and in 1995 in East-Central Nepal. Sparse campaign sites in the Tibetan interior were visited between 1995 and 2007. All vectors are in the International Terrestrial Reference Frame 2000 (ITRF2000). A few GPS-derived vertical velocities are although available in Central Nepal [e.g. *Larson et al.*, 1999; *Fu and Freymueller*, 2012; *Ader et al.*, 2012]. Unfortunately, these data are too noisy to provide sufficiently robust constraints on the parameters estimated in our analysis. Therefore, they are not included in this study.

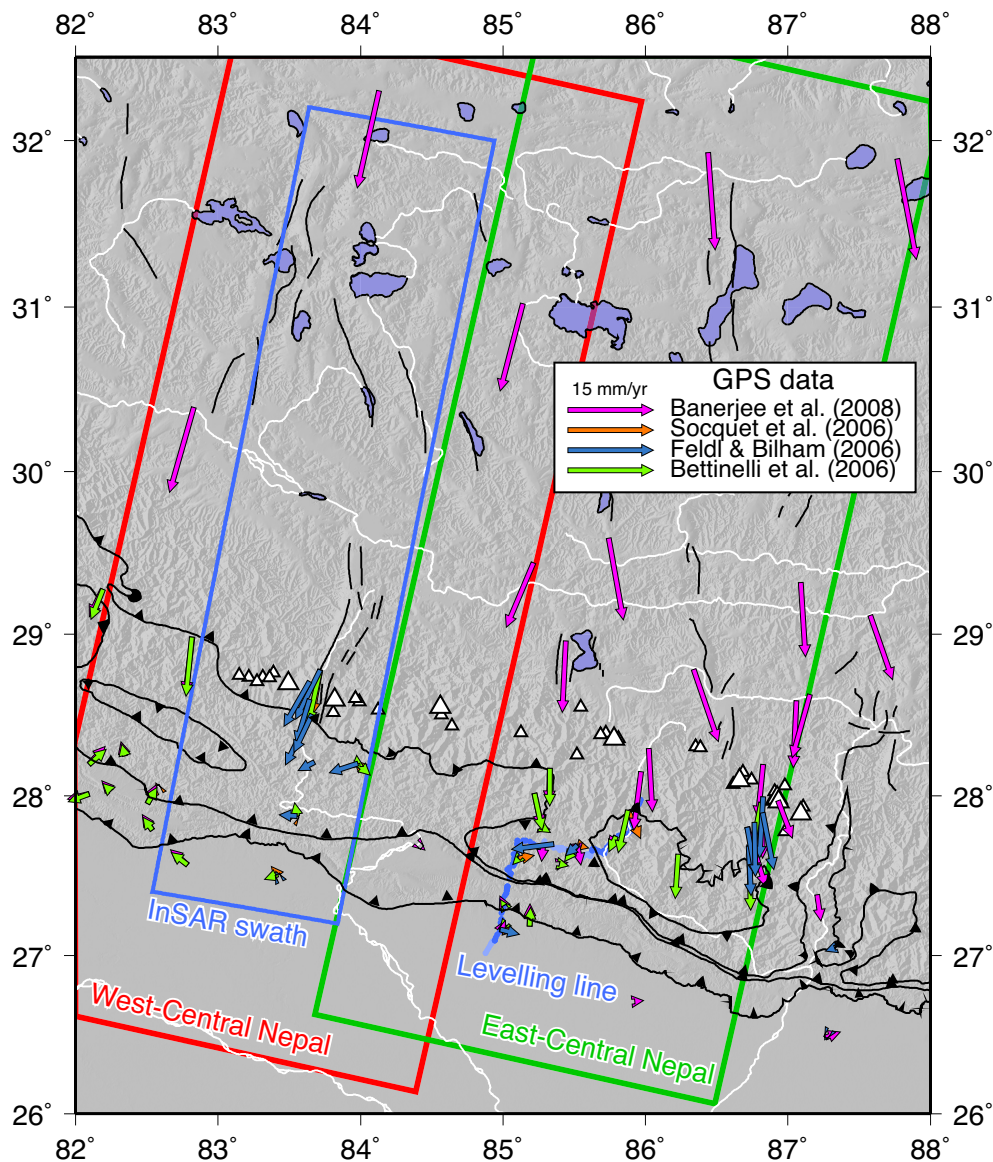


Figure S-10: GPS measurements of the horizontal component of interseismic velocity field across the Himalayan range in Central Nepal. The red and green boxes indicate the location of the two sub-regions of West-Central and East-Central Nepal, respectively. The blue box shows the location of the InSAR track analysed in this study. Leveling profile is also shown in blue. Here, the average of GPS velocity vectors located South of the MFT has been set to zero to plot the velocity field with respect to India.

Inversion procedure

InSAR, GPS and leveling data are assumed to represent different components of the same velocity field, hereafter termed “interseismic”. InSAR and leveling consist of measurements of the vertical component of the interseismic velocity field, whereas GPS constrain the two horizontal components. All GPS and leveling data points were used. However, inversion of InSAR data requires prior data decimation to decrease the number of points and ensure that the inversion is computationally efficient. This was achieved by averaging data points over regions of variable size, with the size of the region depending upon the distance from the location of the band of peak uplift in the Himalaya, following arguments developed by [Grandin et al. \[2009\]](#). The size of the averaging window for InSAR data decimation increases from 5 km within 33 km of the peak uplift, to 10 km between 33 km and 100 km, 20 km between 100 km and 300 km, and finally 40 km above 300 km. This means that data points used in the inversion are more densely spaced near the region of high gradient in the velocity field, and more coarsely spaced further away where measurements are more redundant.

The forward model chosen to account for interseismic deformation is the surface displacement field produced by an infinitely-long dip-slip fault buried at depth in an elastic half-space [[Okada, 1985](#)]. The relevant parameters describing the deformation field are: fault dip, depth of the top of the dislocation, slip rate, fault location, fault strike and rake angle of slip vector. In addition, a translation of the GPS velocity vectors is required to put the different data sets in a common reference frame (for instance stable India). Similarly, we simultaneously invert for a constant offset in the InSAR and leveling data sets. For the inversions, we use the method of [Tarantola and Valette \[1982\]](#). The method allows to invert for one or several parameters simultaneously, including those parameters that have a non-linear dependency upon the data vector (i.e. the geometric parameters).

The data set is split into two regions in East-Central Nepal (InSAR and GPS) and West-Central Nepal (leveling and GPS) that are examined separately (Figure S-10). Only GPS vectors within 140 km from the centre of the two profiles have been taken into account for the inversions. In both regions, the strike of the fault is assumed to follow the trend of the faults outcropping at the surface (N110°E), which is also parallel to the trend of the microseismicity detected along the mountain range throughout Central Nepal (Figure 1). In West-Central Nepal, the fault is assumed to be purely dip-slip, which yields a convergence direction of N10°E, whereas in East-Central Nepal the fault is given a slight right-lateral component, yielding a convergence direction of N05°E. This difference accounts for the rotation of GPS vectors due to internal deformation in Tibet [e.g. [Bollinger et al., 2004](#)]. These parameters are fixed because their influence on the data is marginal (i.e. they cannot be constrained precisely from the data).

We first attempted to invert simultaneously for fault location, depth, dip, and slip rate using jointly InSAR and GPS in West-Central Nepal, and leveling and GPS in East-Central Nepal, respectively. However, inversion results are highly dependent on the relative weight of vertical versus horizontal velocity data. To tackle this difficulty, we inverted separately individual data sets, and performed a systematic parameter exploration to assess how much of each parameter can be reliably constrained by each data set. We chose to explore fault dip and fault depth, while fault latitude and slip rate were left free (Figure S-11). We found that inversion of GPS data provides a good constraint on the slip rate (18 mm/yr), a fair constraint on fault depth, but no constraint on fault dip. In contrast, the leveling data provides a poor constraint on slip rate, fault dip, and favors a fault buried at a depth greater than that required to fit the GPS (25 km versus 18 km). Similarly, InSAR data favors a somewhat deeper fault depth (24 km), and has small sensitivity to slip rate. However, the acceptable interval for fault dip is better constrained than for leveling or GPS, and InSAR data is best fit with a fault dipping at 6.5°. As expected, the fault location is highly sensitive to the location of the peak uplift in the vertical velocity field. On the other hand, the smooth horizontal velocity field does not allow to constrain precisely the location of the fault tip.

Joint vertical/horizontal inversions are expected to provide intermediate solutions in the parameter space between optimal solutions obtained from individual data sets. The difference between the solutions obtained with vertical-only or horizontal-only inversions might be partly due to inadequate assumptions in the forward model, such as an oversimplification of the fault geometry [e.g. [Feldl and Bilham, 2006](#)] or the exclusion of scenarios involving a depth-varying rigidity in the elastic half-space [[Larson et al., 1999](#)]. However, we notice that the ability of the vertical data set to constrain a model

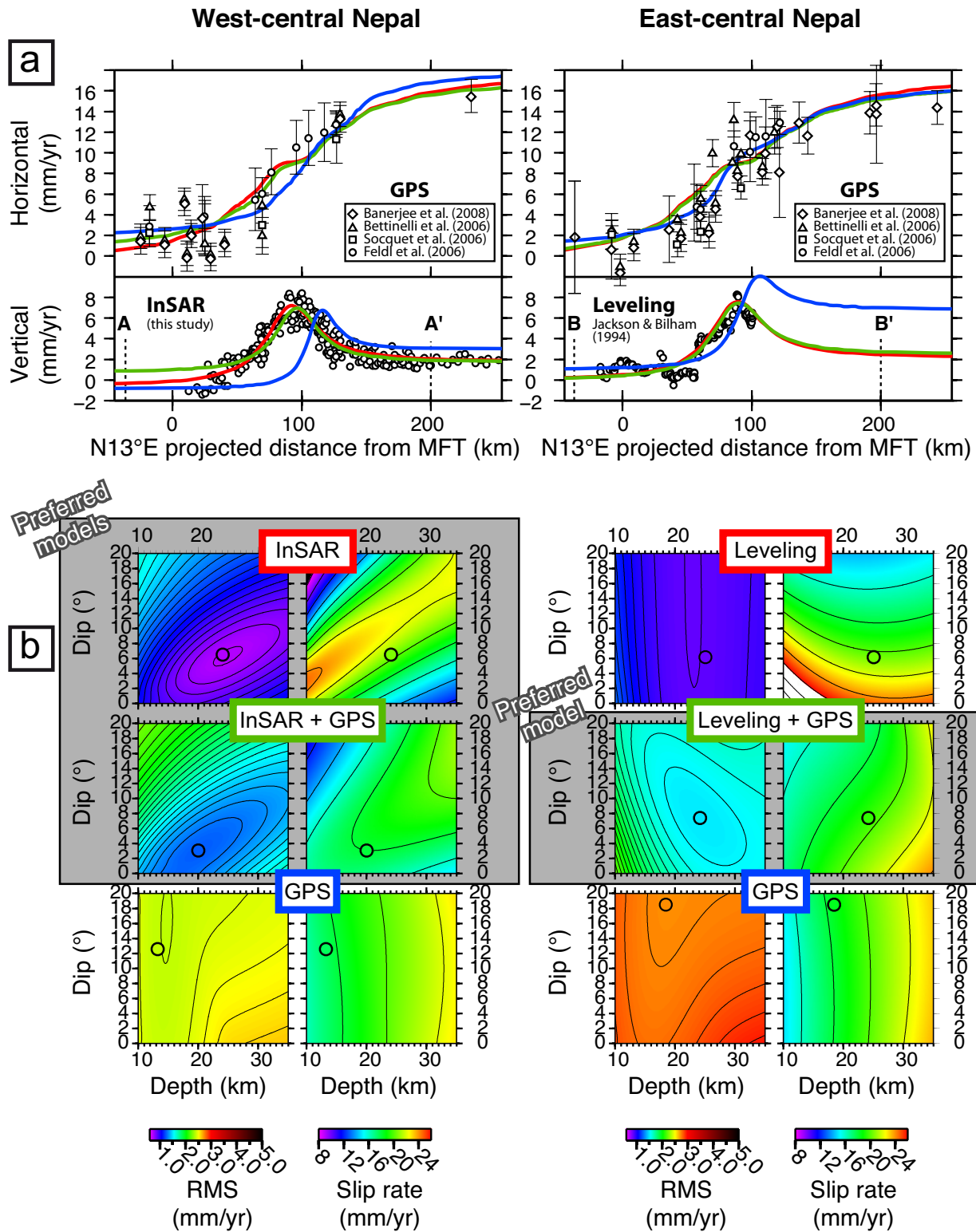


Figure S-11: (a) Horizontal (top) and vertical (bottom) components of interseismic velocity field across the Himalaya in West-Central Nepal (left) and East-Central Nepal (right). The location of profiles is indicated by the red and green boxes in Figure S-10. (b) Exploration of fault parameters using a dislocation model for the two sub-regions using different data sets as input for the inversions. For each given depth and dip of the dislocation, we invert for the optimal fault slip rate and fault location along the profile. Top panels show inversion results using vertical data only (InSAR or leveling), bottom panels show inversion results using horizontal data only (GPS), and middle panels are for joint inversion of horizontal and vertical data. In each panel, the left plot is the root-mean-square (RMS) of the residual, and the right plot is the slip rate determined for each inversion. Color dots indicate the minimum RMS location for the simultaneous inversion of the full set of parameters. Horizontal and vertical surface velocity fields predicted by each inverted fault model are shown in (a). Red: vertical only; blue: horizontal only; green: vertical and horizontal. The preferred models are highlighted by a grey box.

that is capable of explaining the distribution of horizontal velocities is much better than the opposite (i.e. a model determined using inversion of the horizontal velocity field performs poorly in the prediction of the vertical velocity field observed otherwise). This could suggest that horizontal data has less intrinsic ability than vertical data to constrain certain model parameters. This is well captured by the calculation of the variance reduction achieved by a model determined by inversion of separate data sets (Table T-1 and Figure S-11).

In West-Central Nepal, the model obtained by inverting only the InSAR data leads to variance reduction of the GPS data by 56.5%, which is near to the maximum 60.6% achieved by an inversion using GPS only. On the contrary, the “best model” determined by GPS actually increases the variance in the InSAR data by 38%, which corresponds to a degradation of the fit to the data with respect to a null model. Similarly, in East-Central Nepal, a maximum reduction of the variance of the GPS data of 53.3% is obtained by inverting the GPS data only, which is similar to the 50.6% obtained if one inverts the leveling data only. On the contrary, the “best model” deduced from GPS only reduces the variance of the leveling by 37.4%, compared to a maximum variance reduction of 62.2% achieved when inverting the leveling data only. The main reason behind this observation is the poorer constraint on the location of the tip of the fault (both its depth and its location along the profile) provided by GPS, combined with an insensitivity to fault dip. In other words, models derived from GPS predict a peak uplift that may be significantly mislocated with respect to the peak uplift measured by InSAR or leveling, thus leading to a poor fit to the vertical data (see Figure S-11a for a comparison of modeled velocity profiles for the different inversions). In addition, the uneven spatial distribution of GPS stations, as well as the significant scatter among the different data sets, make it difficult to constrain the presence of subtle changes in the North-South gradient of horizontal velocity, which are the key features that allow to constrain geometric parameters of the underlying dislocation from horizontal GPS measurements.

West-central Nepal

	InSAR	GPS						
RMS data	1.9	6.1						
Ndata	268	41						
Data used in inversion	Dip (°)	Depth (km)	Slip rate (mm/yr)	RMS InSAR (mm/yr)	% variance reduction	RMS GPS (mm/yr)	% variance reduction	RMS Total (mm/yr)
InSAR	6.5	24.1	20.6	0.7	60.6	2.7	56.5	-
InSAR+GPS	3.0	20.0	18.0	0.8	56.4	2.5	58.5	1.3
GPS	12.6	13.3	17.5	2.6	-38.2	2.4	60.6	-

East-central Nepal

	Levelling	GPS						
RMS data	2.4	5.9						
Ndata	170	56						
Data used in inversion	Dip (°)	Depth (km)	Slip rate (mm/yr)	RMS levelling (mm/yr)	% variance reduction	RMS GPS (mm/yr)	% variance reduction	RMS Total (mm/yr)
Lev	6.2	25.1	20.5	0.9	62.2	2.9	50.6	-
Lev+GPS	7.4	24.2	19.6	0.9	63.1	2.9	50.6	1.5
GPS	18.5	18.5	18.4	1.5	37.5	2.7	53.4	-

Figure T-1: Inversion results for West-Central Nepal (top) and East-Central Nepal (bottom). RMS data is the variance of the original data. Ndata: number of data points. % variance reduction indicates the performance of each inverted model to explain the variance of the original data. The preferred models are highlighted by a grey box.

Therefore, a joint inversion of horizontal (GPS) and vertical (InSAR or leveling) velocity measurements can be significantly disturbed by inadequate GPS station distribution, or errors/biases in GPS measurements at a few individual stations. Unfortunately, these pitfalls are difficult to avoid in West-Central Nepal, where the different GPS data sets in the area of maximum horizontal velocity gradient (approximately 70 km North of the MFT) show considerable scatter, with velocities spreading between 2 mm/yr and 8 mm/yr with respect to stable India within a distance of 10 km (see Figures S-10 and S-11a). Therefore, in order to account for a probable underestimation of uncertainty in the GPS data, the weight of GPS data with respect to the InSAR data has to be reduced in the joint InSAR–GPS inversions. As a result, our preferred solution in West-Central Nepal lies between model parameters obtained

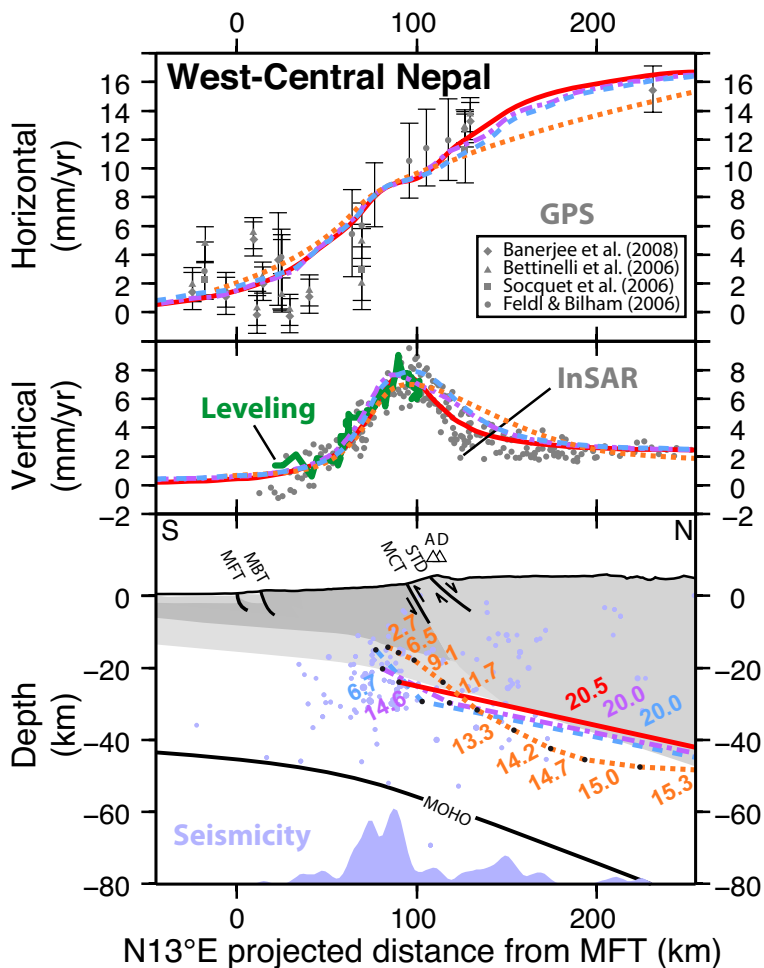


Figure S-12: Horizontal (top) and vertical (bottom) components of interseismic velocity field across the Himalaya in West-Central Nepal. Leveling data from East-Central Nepal is also shown in green for comparison. Light blue dots in the bottom panel show the 2000–2008 seismicity from the NSC catalog. Three different 2D dislocation models are compared, with the cross-sections showing the corresponding geometry and slip rates of sub-faults. Red: best one-dislocation model determined from this study. Purple and blue: two-dislocation models with a deep shallow-dipping dislocation, and a shallower, steeper dislocation with lower slip rate. Orange: model proposed by *Feldl and Bilham* [2006] deduced from boundary-element modeling of GPS data. The models involving more than one dislocation are considered as representative of modeling strategies including the possibility of slip on the deeper portion of the mid-crustal ramp. The horizontal component of the predicted deformation is only marginally different among the different models, i.e. smaller than the uncertainty on the measurement. This suggests that horizontal velocity measurement are insufficient to discriminate between the different models. In contrast, the vertical velocity profiles predicted by the three models differ significantly. Models with variable dip and slip rate predict a slow decay of the uplift rate toward the North away from the peak uplift. These “long-tailed” distributions are inadequate to reproduce the quasi-symmetrical uplift peak deduced from InSAR measurements.

with the joint InSAR–GPS inversion with even weighting of InSAR and GPS (dip=3°; depth=20 km; slip rate=18 mm/yr), and those obtained with the InSAR-only inversion (dip=7°; depth=24 km; slip rate=21 mm/yr). On the contrary, GPS data in East-Central Nepal appear to be well distributed (probably due to the more northerly location of the High range compared to West-Central Nepal) and yield a model in reasonable agreement with leveling measurements in the same area. Therefore, the result of a joint inversion of GPS and leveling is chosen as the preferred model in East-Central Nepal (dip=7°; depth=24 km; slip rate=20 mm/yr). Our preferred models are highlighted in grey in Figure S-11 and Table T-1. The corresponding fault geometries are shown in the cross-sections of Figure 2. We note that the locking depths determined from our various inversions (20–24 km) fall within the values obtained by previous studies in Central Nepal [*Bettinelli et al.*, 2006; *Socquet et al.*, 2006; *Feldl and Bilham*, 2006; *Banerjee et al.*, 2008].

We have also tested alternative models involving more than one dislocation, which could account for a more complex fault geometry, and include possible interseismic slip on the deep part of the mid-crustal ramp. However, the parameter space for such models cannot be explored exhaustively. In Figure S-12, we present three models representative of two alternative modeling strategies, using the data set of West-Central Nepal (InSAR and GPS) to compare predicted and observed velocity profiles. In the first model (in purple in Figure S-12), two dislocations are included: a deep 6°-dipping dislocation of semi-infinite width with a prescribed slip rate of 20 mm/yr connected at 30 km depth with a shallower, steeper dislocation reaching 20 km depth. The dip of the shallow dislocation (15°) is fixed such that the updip projection of the dislocation at the surface roughly corresponds to the MFT. We invert for the slip rate on the shallow dislocation and for the latitudinal location of the pair of dislocations. The best model yields a null slip on the shallower dislocation and a tip for the steeper dislocation located beneath the uplift peak. This means that a single dislocation provides the best fit for this inversion (albeit yielding a poor fit to the data compared to the optimal shallower dislocation model described above and in the main text). However, a strong trade-off is found between the two inverted parameters: the lower the latitude, the lower the inverted slip rate on the mid-crustal dislocation. This shows that the slip rate must be low South of the peak uplift measured by InSAR. To overcome this difficulty,

we arbitrarily fixed the latitude of the dislocation pair so that the upper dislocation is located roughly beneath the peak uplift, which yields an inverted slip rate on the shallow dislocation of 14.6 mm/yr. Such a model could be compatible with partial locking on the deeper part of the mid-crustal ramp. The same behaviour is observed if the dip of the shallowest dislocation is set to 30° between 30 km and 15 km depth, thus simulating the presence of the mid-crustal ramp. For this second model, we also find a reduced slip rate of 6.7 mm/yr on the mid-crustal ramp (in blue in Figure S-12). The same results are obtained when trying to determine the optimal depth and latitudinal location of a fault including one kink (from 6° to 30° dip), divided into several segments to allow for a tapered slip profile on the fault. The best fit to the data is obtained when the deep, shallow-dipping part of the dislocation coincides with our single dislocation model that provides the best fit (Figure 2), and when the shallower, steeply-dipping segments have a null slip.

In a third model (in orange in Figure S-12), *Feldl and Bilham* [2006] proposed a more complex modeling of the creeping section of MHT. In this model, tapering of the interseismic slip rate towards the surface was determined by boundary-element modeling of horizontal GPS data given a prescribed sigmoidal geometry of the fault at depth. The deepest flat-lying elements slip at a rate > 15 mm/yr (up to 25 mm/yr beyond 500 km from the tip of the creeping fault).

All the models discussed here predict similar horizontal velocity profiles, in agreement with observations (Figure S-12, top). This again suggests that knowledge of the horizontal component of the interseismic velocity field is insufficient to precisely constrain the geometry of the underlying fault system. However, the models involving several dislocations always seem to produce a broad peak of uplift, thus failing to reproduce the rapid decay of the vertical uplift velocity toward the North (Figure S-12, middle). In contrast, a single-dislocation model succeeds in fitting the nearly symmetrical shape of the uplift peak, which supports the existence of a sharp transition between a deep creeping section and a shallower locked section of the fault. Because the leveling profile is limited to the Nepal territory, this ambiguity among different models could not be resolved in previous studies [e.g. *Jackson and Bilham, 1994*]. Therefore, the single dislocation model is our preferred one.

Seismic catalogue

The National Seismological Centre (NSC) from the Nepalese Department of Mines and Geology monitors the seismicity using a network of 21 short-period stations deployed within the frame of a long lasting collaboration with CEA/DASE (France). The seismic events are located using a 3 layers 1D-velocity model, characterizing the velocities for depths of 0–23 km, 23–55 km and more than 55 km with P -wave velocities respectively of 5.6, 6.1 and 8.1 km/s [Pandey, 1985]. The seismic events located within the network, which is the case for the mid-crustal events reported here on the cross sections through the High Himalayan range, are located within 1σ confidence ellipses typically smaller than 10–15 km, with less than 10 km uncertainty on their depths [e.g. Pandey et al., 1995]. Note that the mid-crustal cluster is more diffuse in West Central Nepal than in East Central Nepal (Figure 2), which is most probably related to the lower station density and azimuth coverage. A temporary experiment with 3 additional seismic stations deployed from July to December 1995 around the mid-crustal cluster North of Kathmandu suggested that the hypocentral depths determined on routine basis may be overestimated in this region by 5 km [Pandey et al., 1999]. Although similar biases could also affect the hypocentral depths in West-Central Nepal, this result has not been taken into account to correct any depths in Figure 2.

River denudation profiles

Lavé and Avouac [2001] have determined riverbed erosion profiles along major rivers of Central Nepal crossing the active tectonic structures of the Himalayan orogen. In lowland Nepal, incision through the rising anticline associated with the MFT gives rise to a series of nested strath terraces that were used to determine the uplift rate. At higher elevation, modern channel topographic slope and width were used to infer denudation rates via an empiric relationship involving river discharge and watershed surface area. The resulting profiles show a bimodal distribution of erosion in Central Nepal. A first sharp peak (maximum ~ 10 mm/yr) is associated with the frontal outbreak of MHT near the MFT. A second broader peak (maximum ~ 7 mm/yr) located ~ 100 km inland in the High Himalaya is loosely collocated with the surface trace of the MCT. Two rivers profiles are of particular interest for our study. (1) The Kali Gandaki river drains the Thakkhola graben, and follows our InSAR profile in West-Central Nepal. (2) The upper part of the leveling profile in East-Central Nepal corresponds to the trace of the Sun Kosi km North of the MFT, respectively. In Figure 2, we have represented the average erosion profile deduced from stacking the 6 profiles, and we have set the location of the peak in the High Himalaya to fit the location of the peak deduced from the two rivers in their respective sub-region. In Figure 3, we have represented the expected erosion profile for three models of mountain growth (black curves). The profile in Figure 3A is from Cattin and Avouac [2000], who predict that a prominent uplift peak should be located where the MFT intersects the surface (first peak), while another broader uplift peak in the High Himalaya occurs above the mid-crustal ramp within the MHT (second peak). In Figure 3B, we have assumed that half of the convergence is accommodated by thrusting along the MFT (first peak), while the remaining convergence is accommodated by out-of-sequence thrusting near the surface trace of the MCT (second peak). In Figure 3C, the uplift peak above the ramp predicted by the steady-state model of Cattin and Avouac [2000] has been shifted to the North above an abandoned ramp, in order to simulate the impact of a recent southward migration of the mid-crustal ramp whose effect on the long-term uplift profile would not yet be expressed in riverbed morphology.

References

- Ader, T., J.-P. Avouac, J. Liu-Zheng, H. Lyon-Caen, L. Bollinger, J. Galetzka, J. Genrich, M. Thomas, K. Chanard, S. N. Sapkota, S. Rajaure, P. Shrestha, L. Ding, and M. Flouzat (2012), Convergence rate across the Nepal Himalaya and interseismic coupling on the Main Himalayan Thrust: Implications for seismic hazard, *J. Geophys. Res.*, *117*, B04403, doi:10.1029/2011JB009071.
- Banerjee, P., R. Bürgmann, B. Nagarajan, and E. Apel (2008), Intraplate deformation of the Indian subcontinent, *Geophys. Res. Lett.*, *35*, L18301, doi:10.1029/2008GL035468.
- Bettinelli, P., J.-P. Avouac, M. Flouzat, F. Jouanne, L. Bollinger, P. Willis, and G. J. Chitrakar (2006), Plate motion of India and interseismic strain in the Nepal Himalaya from GPS and DORIS measurements, *Journal of Geodesy*, *80*, 567–589, doi:10.1007/s00190-006-0030-3.
- Bollinger, L., J. P. Avouac, R. Cattin, and M. R. Pandey (2004), Stress buildup in the Himalaya, *J. Geophys. Res.*, *109*(B18), B11405, doi:10.1029/2003JB002911.
- Cattin, R., and J. P. Avouac (2000), Modeling mountain building and the seismic cycle in the Himalaya of Nepal, *J. Geophys. Res.*, *105*, 13,389–13,408, doi:10.1029/2000JB900032.
- Davidson, G. W., and R. Bamler (1999), Multiresolution phase unwrapping for SAR interferometry, *IEEE Transactions on Geoscience and Remote Sensing*, *37*, 163–174, doi:10.1109/36.739150.
- Doin, M.-P., S. Guillaso, R. Jolivet, C. Lasserre, F. Lodge, G. Ducret, and R. Grandin (2011), Presentation of the small baseline NSBAS processing chain on a case example: the Etna deformation monitoring from 2003 to 2010 using Envisat data, in *Proceedings of the European Space Agency (ESA) "Fringe" Symposium, Frascati, Italy*.
- Ducret, G., M. P. Doin, R. Grandin, C. Lasserre, and S. Guillaso (2011), DEM corrections before unwrapping in a small baseline strategy for insar time series analysis, in *Proceedings of the IEEE International Geoscience and Remote Sensing Symposium, Vancouver, Canada*.
- Farr, T. G., P. A. Rosen, E. Caro, R. Crippen, R. Duren, S. Hensley, M. Kobrick, M. Paller, E. Rodriguez, L. Roth, D. Seal, S. Shaffer, J. Shimada, J. Umland, M. Werner, M. Oskin, D. Burbank, and D. Alsdorf (2007), The Shuttle Radar Topography Mission, *Reviews of Geophysics*, *45*, RG2004, doi:10.1029/2005RG000183.
- Feldl, N., and R. Bilham (2006), Great Himalayan earthquakes and the Tibetan plateau, *Nature*, *444*, 165–170, doi:10.1038/nature05199.
- Fu, Y., and J. T. Freymueller (2012), Seasonal and long-term vertical deformation in the Nepal Himalaya constrained by GPS and GRACE measurements, *J. Geophys. Res.*, *117*, B03407, doi:10.1029/2011JB008925.
- Gatelli, F., A. M. Guarnieri, F. Parizzi, P. Pasquali, C. Prati, and F. Rocca (1994), Wavenumber shift in SAR interferometry, *IEEE Transactions on Geoscience and Remote Sensing*, *32*, 855–865, doi:10.1109/36.298013.
- Grandin, R., A. Socquet, R. Binet, Y. Klinger, E. Jacques, J. B. de Chabalier, G. C. P. King, C. Lasserre, S. Tait, P. Tapponnier, D. A., and P. P. (2009), September 2005 Manda Hararo-Dabbahu rifting event, Afar (Ethiopia): Constraints provided by geodetic data, *J. Geophys. Res.*, *114*(B08404), doi:10.1029/2008JB005843.
- Jackson, M., and R. Bilham (1994), Constraints on Himalayan deformation inferred from vertical velocity fields in Nepal and Tibet, *J. Geophys. Res.*, *99*, 13,897, doi:10.1029/94JB00714.
- Jolivet, R., R. Grandin, C. Lasserre, M.-P. Doin, and G. Peltzer (2011), Systematic InSAR tropospheric phase delay corrections from global meteorological reanalysis data, *Geophys. Res. Lett.*, *38*, L17311, doi:10.1029/2011GL048757.
- Larson, K. M., R. Bürgmann, R. Bilham, and J. T. Freymueller (1999), Kinematics of the India-Eurasia collision zone from GPS measurements, *J. Geophys. Res.*, *104*, 1077–1094, doi:10.1029/1998JB900043.
- Lavé, J., and J. P. Avouac (2001), Fluvial incision and tectonic uplift across the Himalayas of central Nepal, *J. Geophys. Res.*, *106*, 26,561–26,592, doi:10.1029/2001JB000359.
- Okada, Y. (1985), Surface deformation due to shear and tensile faults in a half space, *Bull. Seismol. Soc. Am.*, *75*(4), 1135–1154.
- Pandey, M., R. P. Tandukar, J.-P. Avouac, J. Vergne, and T. Heritier (1999), Seismotectonics of the Nepal Himalaya from a local seismic network, *Journal of Asian Earth Sciences*, *17*, 703–712, doi:10.1016/S1367-9120(99)00034-6.
- Pandey, M. R. (1985), Seismic model of central and eastern lesser Himalaya of Nepal, *Journal of Nepal Geological Society*, *3*, 1–11.
- Pandey, M. R., R. P. Tandukar, J. P. Avouac, J. Lave, and J. P. Massot (1995), Interseismic strain accumulation on the Himalayan Crustal Ramp (Nepal), *Geophys. Res. Lett.*, *22*, 751–754, doi:10.1029/94GL02971.
- Pinel-Puysségur, B., R. Michel, and J.-P. Avouac (2011), Multi-link SAR interferograms: enhancement of a wrapped interferometric database, in *Proceedings of the IEEE International Geoscience and Remote Sensing Symposium, Vancouver, Canada*.
- Rosen, P. A., S. Henley, G. Peltzer, and M. Simons (2004), Updated Repeat Orbit Interferometry Package Released, *Eos Trans. AGU*, *85*(5), 47–47, doi:10.1029/2004EO050004.
- Socquet, A., C. Vigny, N. Chamot-Rooke, W. Simons, C. Rangin, and B. Ambrosius (2006), India and Sunda plates motion and deformation along their boundary in Myanmar determined by GPS, *J. Geophys. Res.*, *111*(B10), B05406, doi:10.1029/2005JB003877.
- Tarantola, A., and B. Valette (1982), Generalized Nonlinear Inverse Problems Solved Using the Least Squares Criterion, *Rev. Geophys.*, *20*, 219–232.
- Zandbergen, R., M. Otten, P. L. Righetti, D. Kuijper, and J. M. Dow (2003), Routine operational and high-precision orbit determination of envisat, *Advances in Space Research*, *31*, 1953–1958, doi:10.1016/S0273-1177(03)00154-6.